Longitudinal molecular trajectories of diffuse glioma in adults

Barthel, Floris P ; Johnson, Kevin C ; Varn, Frederick S ; Moskalik, Anzhela D ; Tanner, Georgette ; Kocakavuk, Emre ; et al ; Weller, Michael

Abstract: The evolutionary processes that drive universal therapeutic resistance in adult patients with diffuse glioma remain unclear[1,2]. Here we analysed temporally separated DNA-sequencing data and matched clinical annotation from 222 adult patients with glioma. By analysing mutations and copy numbers across the three major subtypes of diffuse glioma, we found that driver genes detected at the initial stage of disease were retained at recurrence, whereas there was little evidence of recurrence-specific gene alterations. Treatment with alkylating agents resulted in a hypermutator phenotype at different rates across the glioma subtypes, and hypermutation was not associated with differences in overall survival. Acquired aneuploidy was frequently detected in recurrent gliomas and was characterized by IDH mutation but without co-deletion of chromosome arms 1p/19q, and further converged with acquired alterations in the cell cycle and poor outcomes. The clonal architecture of each tumour remained similar over time, but the presence of subclonal selection was associated with decreased survival. Finally, there were no differences in the levels of immunoediting between initial and recurrent gliomas. Collectively, our results suggest that the strongest selective pressures occur during early glioma development and that current therapies shape this evolution in a largely stochastic manner.

DOI: https://doi.org/10.1038/s41586-019-1775-1

Originally published at:
Barthel, Floris P; Johnson, Kevin C; Varn, Frederick S; Moskalik, Anzhela D; Tanner, Georgette; Kocakavuk, Emre; et al; Weller, Michael (2019). Longitudinal molecular trajectories of diffuse glioma in adults. Nature, 576(7785):112-120.
DOI: https://doi.org/10.1038/s41586-019-1775-1

LONGITUDINAL MOLECULAR TRAJECTORIES OF DIFFUSE GLIOMA IN ADULTS

The Glioma Longitudinal Analysis (GLASS) Consortium

Floris P. Barthel[1, 2, 52], Kevin C. Johnson[1,52], Frederick S. Varn[1], Anzhela D. Moskalik[1], Georgette Tanner[3], Emre Kocakavuk[1,4], Kevin Anderson[1], Olajide Abiola[1], Kenneth Aldape[5], Kristin D. Alfaro[6], Donat Alpar[7,8], Samirkumar B. Amin[1], David M. Ashley[9], Pratiti Bandopadhayay[10,11], Jill S. Barnholtz-Sloan[12], Rameen Beroukhim[10,11], Christoph Bock[7,13], Priscilla K. Brastianos[14], Daniel J. Brat[15], Andrew R. Brodbelt[16], Alexander F. Bruns[3], Ketan R. Bulsara[17], Aruna Chakrabarty[18], Arnab Chakravarti[19], Jeffrey H. Chuang[1,20], Elizabeth B. Claus[21,22], Elizabeth J. Cochran[23], Jennifer Connelly[23], Joseph F. Costello[24], Gaetano Finocchiaro[25], Michael N. Fletcher[26], Pim J. French[27], Hui Gan[28], Mark R. Gilbert[29], Peter V. Gould[30], Matthew R. Grimmer[24], Antonio Iavarone[31], Azzam Ismail[18], Michael D. Jenkinson[16], Mustafa Khasraw[32], Hoon Kim[1], Mathilde C.M. Kouwenhoven[2], Peter S. LaViolette[23], Meihong Li[1], Peter Lichter[26], Keith L. Ligon[10,11], Allison K. Lowman[23], Tathiane M. Malta[33], Tali Mazor[24], Kerrie L. McDonald[34], Annette M. Molinaro[24], Do-Hyun Nam[35], Naema Nayyar[14], Ho Keung Ng[36], Chew Yee Ngan[1], Simone, P.Niclou[37], Johanna M. Niers[2], Houtan Noushmehr[33], Javad Noorbakhsh[1], D. Ryan Ormond[38], Chul-Kee Park[39], Laila M. Poisson[33], Raul Rabadan[31], Bernhard Radlwimmer[26], Ganesh Rao[6], Guido Reifenberger[40], Jason K. Sa[41], Michael Schuster[7], Brian L. Shaw[14], Susan C. Short[3], Peter A. Sillevis Smitt[27], Andrew E. Sloan[42], Marion Smits[27], Hiromichi Suzuki[43], Ghazaleh Tabatabai[44], Erwin G. Van Meir[45], Colin Watts[46], Michael Weller[47], Pieter Wesseling[2,48], Bart A. Westerman[2], Georg Widhalm[49], Adelheid Woehrer[50], W.K. Alfred Yung[6], Gelareh Zadeh[51], GLASS Consortium, Jason T. Huse[6], John F. de Groot[6], Lucy F. Stead[3], Roel G.W. Verhaak[1¥]

[1]The Jackson Laboratory for Genomic Medicine, Farmington, CT, 06032, USA.
[2]Amsterdam UMC, Vrije Universiteit Amsterdam, Departments of Neurology, Neurosurgery, Pathology, Brain Tumor Center Amsterdam, de Boelelaan 1117, Amsterdam, Netherlands
[3]Leeds Institute of Medical Research at St James's, University of Leeds, LS9 7TF, UK.
[4]DKFZ Division of Translational Neurooncology at the West German Cancer Center, German Cancer Consortium Partner Site & Department of Neurosurgery, University Hospital Essen, 45147 Essen, Germany
[5]National Cancer Institute, Bethesda, MD 20892, USA
[6]Departments of Neuro-Oncology, Neurosurgery, Pathology, Translational Molecular Pathology, The University of Texas MD Anderson Cancer Center, Houston, Texas 77031, USA
[7]CeMM Research Center for Molecular Medicine of the Austrian Academy of Sciences, 1090 Vienna, Austria
[8]1st Department of Pathology and Experimental Cancer Research, Semmelweis University, 1085 Budapest, Hungary
[9]Preston Robert Tisch Brain Tumor Center at Duke, Duke University Medical Center, Durham, North Carolina 27710, USA
[10]Dana-Farber Cancer Institute, 450 Brookline Ave, Boston, MA 02215, USA
[11]Broad Institute, 415 Main Street, Cambridge, MA 02142, USA
[12]Department of Population and Quantitative Health Sciences and Case Comprehensive Cancer Center, Case Western Reserve University School of Medicine, 2103 Cornell Rd, WRB 2-526, Cleveland, Ohio 44106, USA
[13]Department of Laboratory Medicine, Medical University of Vienna, Vienna, Austria

[14]Division of Neuro-Oncology, Massachusetts General Hospital, Boston, MA 02114, USA
[15]Department of Pathology, Northwestern University Feinberg School of Medicine, Chicago IL, 60611, USA
[16]University of Liverpool & Walton Centre NHS Trust, Liverpool, L9 7LJ, UK
[17]Division of Neurosurgery, The University of Connecticut Health Center, Farmington, CT, USA
[18]Leeds Teaching Hospital NHS Trust, St James's University Hospital, Leeds, LS9 7TF, UK
[19]Department of Radiation Oncology, Arthur G. James Hospital/Ohio State Comprehensive Cancer Center, Columbus, OH, 43210, USA
[20]UConn Health, Department of Genetics and Genome Sciences, Farmington, CT, 06030, USA
[21]Yale University School of Public Health, New Haven, CT, 06511, USA
[22]Department of Neurosurgery, Brigham and Women's Hospital, Boston, MA, USA
[23]Departments of Neurology, Pathology, Radiology and Biomedical Engineering, Medical College of Wisconsin, Milwaukee, WI USA
[24]Department of Neurosurgery, University of California San Francisco, CA 94143, USA
[25]Fondazione IRCCS Istituto Neurologico Besta, Milano, Italy
[26]Division of Molecular Genetics, Heidelberg Center for Personalized Oncology, German Cancer Research Consortium, German Cancer Research Center (DKFZ), Heidelberg, Germany
[27]Departments of Neurology, Radiology and Nuclear Medicine, Erasmus MC - University Medical Center Rotterdam, PO Box 2040, 3000 CA Rotterdam, the Netherlands
[28]Olivia Newton-John Cancer Research Institute, Austin Health, Melbourne, Australia
[29]Neuro-oncology Branch, National Institutes of Health, Bethesda, Maryland, 20892, USA
[30]Anatomic Pathology Service, Hôpital de l'Enfant-Jésus, CHU de Québec-Université Laval, Québec QC G1J 1Z4, Canada
[31]Departments of Neurology, Pathology, Cell Biology, Systems Biology and Biomedical Informatics, Institute for Cancer Genetics, Columbia University Medical Center, New York, New York 10032, USA
[32]Cooperative Trials Group for Neuro-Oncology (COGNO) NHMRC Clinical Trials Centre, The University of Sydney, New South Wales, Australia
[33]Departments of Neurosurgery, Public Health Sciences, Henry Ford Health System, Henry Ford Cancer Institute, Detroit, MI 48202, USA
[34]Cure Brain Cancer Biomarkers and Translational Research Group, Prince of Wales Clinical School, UNSW Sydney, Australia
[35]Department of Neurosurgery, Sungkyunkwan University School of Medicine, Samsung Medical Center, Seoul, Korea
[36]Department of Anatomical and Cellular Pathology, The Chinese University of Hong Kong, 1/F, Prince of Wales Hospital, Shatin, Hong Kong
[37]Department of Oncology, Luxembourg Institute of Health, Luxembourg
[38]Department of Neurosurgery, University of Colorado School of Medicine, Aurora, Colorado, 80045, USA
[39]Department of Neurosurgery, Seoul National University College of Medicine, Seoul National University Hospital, Seoul, Korea
[40]Institute of Neuropathology, Heinrich Heine University Düsseldorf, Düsseldorf, Germany
[41]Institute for Refractory Cancer Research, Samsung Medical Center, Seoul, Korea
[42]Department of Neurosurgery, University Hospitals-Case Medical Center, Seidman Cancer Center, and the Case Comprehensive Cancer Center, Cleveland, Ohio 44106, USA
[43]The Hospital for Sick Children, Toronto, ON, M5G1X8, Canada
[44]Interdiscplinary Division of Neuro-Oncology, Hertie Institute for Clinical Brain Research, DKTK Partner Site Tübingen, Eberhard Karls University Tübingen, Germany
[45]Department of Neurosurgery, School of Medicine and Winship Cancer Institute of Emory U University; 1365C Clifton Rd. NE, Atlanta, GA30084, USA

[46]Institute of Cancer Genome Sciences, Department of Neurosurgery, University of Birmingham, UK
[47]Department of Neurology, University Hospital Zurich, Zurich, Switzerland
[48]Princess Máxima Center for Pediatric Oncology, Utrecht, The Netherlands
[49]Department of Neurosurgery, Medical University of Vienna, 1090 Vienna, Austria
[50]Institute of Neurology, Medical University of Vienna, 1090 Vienna, Austria
[51]Division of Neurosurgery, Department of Surgery, University Health Network, Toronto, C Canada.
[52]These authors contributed equally.

[¥] Correspondence to roel.verhaak@jax.org.

ABSTRACT

The evolutionary processes that drive universal therapeutic resistance in adult patients with diffuse glioma remain unclear. Here, we analyzed temporally separated DNA sequencing data and matched clinical annotation from 222 patients with glioma. Through mutational and copy number analyses across the three major subtypes of diffuse glioma in adults, we observed that driver genes detected at initial disease were retained at recurrence, while there was little evidence of recurrence-specific gene alterations. Treatment with alkylating-agents resulted in a hypermutator phenotype at different rates across glioma subtypes, and hypermutation was not associated with differences in survival. Acquired aneuploidy was frequently detected in recurrent gliomas characterized by presence of an IDH mutation but without 1p/19q codeletion and further converged with acquired cell cycle alterations and poor outcomes. We show that the clonal architecture of each tumor remains similar over time and that absence of clonal selection was associated with increased survival. Finally, we found that neoantigens were exposed to stable selective pressures throughout a tumor's progression. Our results collectively suggest that the strongest selective pressures occur early during glioma development and that current therapies shape this evolution in a largely stochastic manner.

INTRODUCTION

Diffuse glioma is the most common malignant brain tumor in adults. Nearly all gliomas relapse despite treatment with surgery, radiotherapy, and chemotherapy. The genomic and molecular landscape of glioma at diagnosis has been extensively characterized through The Cancer Genome Atlas (TCGA) and other cancer genomics projects[1-7]. These efforts have led to the identification of the most significantly somatically altered genes and define three major glioma subtypes based on alterations known to occur early in gliomagenesis, including IDH mutation (*IDH1* or *IDH2*) and combined chromosome 1p/19q deletion. While somatic genomic characterization of glioma at diagnosis has classified patients with distinct clinical outcomes[8,9], there remains a poor systematic understanding of how the glioma genetic landscape evolves over time and in response to therapy.

Intratumoral heterogeneity is a well-recognized characteristic of gliomas and results from various pressures such as a dynamic tumor microenvironment, clonal competition and genetic drift [10-13]. External pressures after diagnosis via a limited availability of nutrients, oxygen, or the toxic effects of chemotherapy and radiation therapy, may further shape tumor evolution. Tumors are thought to circumvent these growth bottlenecks via dynamic competition of subclones resulting in the most favorable environment for tumor sustenance[14]. Recent studies have suggested that stochastic changes in clone frequency (i.e. neutral evolution) may further contribute to the observed intratumoral heterogeneity[15]. Extrinsic forces such as immune surveillance can also influence tumor evolution by eliminating tumor cells with immunogenic mutations[16]. However, knowledge of these processes has focused primarily on gliomas at initial diagnosis and a better understanding of evolutionary dynamics over time is needed to develop strategies aimed at delaying or preventing the onset of tumor progression.

To investigate clonal dynamics over time and in response to therapeutic pressures, we established the Glioma Longitudinal Analysis (GLASS) Consortium. GLASS is a community-driven effort that seeks to overcome the logistical challenges in constructing adequately powered longitudinal genomic glioma datasets by pooling datasets from patients treated at institutions worldwide. We have generated longitudinal mutation, copy number, clonal frequency, and neoantigen profiles from gliomas across the three molecular glioma subtypes. We leveraged the genomic datasets to identify the distinct molecular processes active at initial and recurrent time points. These analyses identified few common features of glioma evolution across subtypes and instead, a multitude of different and patient-specific trajectories of genomic alterations. The acquisition of specific alterations are rarely drivers of recurrence, thus firmly

rejecting the hypothesis that a simple, shared evolutionary program drives glioma recurrence in most or all patients.

RESULTS

GLASS cohort

We pooled longitudinal DNA sequencing datasets from patients treated at 35 hospitals (Supplementary Table 1). All data was processed using standardized pipelines for genomic data analysis and clinical data aggregation. A grand total of 288 patients were evaluated for inclusion. Various quality control metrics included: filtering samples based on patient-level fingerprint matching, minimum sequencing coverage, and copy number segmentation noise (Extended Data Fig. 1). We classified all tumor samples according to molecular markers into three major glioma subtypes: 1. IDH-mutant and 1p/19q codeleted (IDHmutant-codel) 2. IDH-mutant without 1p/19q codeletion (IDHmutant-noncodel) and 3. IDH wild type (IDHwt) to best align with the World Health Organization classification of Central Nervous System tumors [8,9]. After applying filters, 222 patients (n = 134 IDHwt, n = 63 IDHmutant-noncodel, n = 25 IDHmutant-codel) with high-quality data in at least two time points remained. For each patient we selected two time-separated tumor samples, henceforth initial and recurrence, for further analysis. A detailed overview of patient and sample selection can be found in the Supplementary Text and Extended Data Fig. 1.

Temporal changes in glioma mutational rates and processes

To establish a basic understanding of glioma evolution, we evaluated changes in mutational rates and processes over time. Mutation rates in initial tumors were comparable with previously reported rates [4,5]: 2.20 mutations (single-nucleotide variants and small insertions/deletions) per Megabase (Mutations/Mb) for IDHmutant-codels; 2.52 Mutations/Mb for IDHmutant-noncodels; and 2.85 Mutations/Mb for IDHwt glioma (Fig. 1a; Extended Data Fig. 2a). Excluding DNA hypermutation cases (> 10 Mutations/Mb, n = 35), the mutation rate increased after recurrence in 70% of the cohort. There was a significant increase in mutation rate at recurrence across all three subtypes independent of hypermutator status (Extended Data Fig. 2a). To study changes during tumor progression, we separated mutations and copy number events into three fractions depending on whether they were called in the initial only, recurrence only, or were shared. Interestingly, we did not detect any differences in mutation rates between subtypes in the private fractions, and subtype differences in mutation rate were largely determined by the

shared fraction (Extended Data Fig. 2b). Patient age at diagnosis was strongly associated with the shared mutational rate and only weakly with the rate of mutations private to the initial tumor (Extended Data Fig. 2c). On average, tumors with longer time to recurrence had slightly higher mutation rates (Extended Data Fig. 2d).

These characteristic differences suggested the activity of mutational processes only in the initial tumor, only in to the recurrent rumor, or throughout the life of the tumor. We therefore classified mutations in each fraction according to the Catalogue of Somatic Mutations in Cancer (COSMIC) signature database[17]. As expected, signature activity was closely related to subtype and fraction (Fig. 1b, Extended Data Fig. 3a). Signature 1 (aging) was nearly always the dominant signature amongst shared mutations in IDHwt tumors, whereas the shared fraction in IDHmut-noncodel and IDHmut-codel tumors - tumor subtypes associated with a younger age of diagnosis - additionally showed a strong presence of signature 16 (unknown etiology). Signatures 3 (double strand break repair) and 15 (mismatch repair) along with signature 8 (unknown etiology) were mostly confined to the private fractions, suggesting that these processes were of lesser importance to tumor maintenance and that aging is the primary mechanism by which tumor sustaining mutations arise.

Treatment of glioma includes alkylating agents that can induce post-treatment hypermutation[18-20]. Indeed, we observed a striking enrichment of signature 11 (nucleotide excision repair) in recurrent tumors with a mutational load exceeding 10 Mutations/Mb and treated with alkylating agents, consistent with reports describing this phenomenon in IDHmut-noncodel tumors (Fig. 1a, Extended Data Fig. 3b)[20]. Here we observed treatment-associated hypermutation in all three subtypes but most frequently among IDHmutant-noncodels (15 out 32, 47%), followed by IDHmutant-codels (2 out of 8, 25%), and IDHwt gliomas (16 of 99, 16%). The difference in the proportion of hypermutation events was significantly different between the three glioma subtypes (Fig. 1c, Fisher's exact-test P = 2.0e-03), possibly indicating that IDHmutant-noncodels may be most sensitive to developing a hypermutator phenotype[21].

Hypermutation following alkylating agent therapy has been suggested to associate with malignant progression[20]. We did not find a difference in overall survival between alkylating agent-treated hypermutators and alkylating agent-treated non-hypermutators independent of age, subtype, and *MGMT* methylation status (Fig. 1d, Supplementary Table 2a-b). In order to further assess the pathogenicity of acquired mutations, we studied their clonality[22]. Newly acquired clonal mutations have penetrated a majority of cancer cells over the short period of time (i.e. a selective sweep) between initial and recurrence and could possibly drive tumor growth[23]. In contrast, acquired subclonal mutations are present in a subset of cancer cells and

are thus less likely to have driven malignant transformation. Previous reports have suggested that mutations acquired due to alkylating agent-associated hypermutation are often clonal[24]. We found that in 48% of hypermutated tumors a majority of the recurrence-only mutations were clonal, potentially reflecting cases where a selective sweep occurred (Extended Data Fig. 4a). A survival analysis comparing IDHmut-noncodel hypermutators with predominantly clonal mutations to those with predominantly subclonal mutations did not show any significant differences (log-rank test $P = 0.38$, Extended Data Fig. 4b). Alkylating agents such as temozolomide (TMZ) prolong survival of adult patients with a glioma[25,26]. Our results show that hypermutation following treatment with alkylating agents is common and demonstrate that overall survival of patients with a hypermutated glioma does not differ from patients treated with alkylating agent and with a non-hypermutated glioma, reflecting the overall benefit of this chemotherapy.

Quantifying selective pressures during glioma evolution

If mutational patterns are different across time points and subtypes, then changes in clonal architecture might be expected at recurrence. To determine selection over time we used TITAN and PyClone to cluster copy number changes and mutations based on their cancer cell fraction (CCF)[27,28]. CCF values represent the fraction of cancer cells harboring a given alteration and can be used in estimating the relative timing of events, since alterations that are present in a subset of cancer cells likely occurred later than events present in all cancer cells (Fig. 2a). It is not possible to accurately time alterations of equal CCF, as cells with both alterations may have completely outcompeted cells with only the earlier occurring alteration. This is especially important to consider with respect to recurrent tumors where surgery and treatment may have removed many cells from the tumor. We found that nearly all patients (98%) demonstrated a dominant cluster of mutations that persisted between the initial tumor and recurrence with a CCF of at least 25% and in majority more than 50%, reflecting a major clone (Extended Data Fig. 5a). To determine changes in clonal dominance over time we ranked clusters within each sample according to their CCF and found that the major tumor-driving cluster remained a top-ranked cluster throughout the course of disease and regardless of treatment (Fig. 2b, Extended Data Fig. 5b-d). These results suggested that the clone driving the initial tumor continued to be the dominant force driving recurrence.

To deepen our assessment of selective pressures in glioma progression, we next evaluated selection in initial and recurrent tumors by determining the normalized ratio between non-synonymous and synonymous mutations (dN/dScv)[29]. Briefly, if the number of non-synonymous mutations exceeds expectations (dN/dS > 1) these mutations are thought to be

positively selected for, whereas a dN/dS significantly below one indicates negative selection. We found evidence for positive selection at both time points despite differences between subtypes (Fig. 2c). Separating mutations into subsets of initial-only, shared and recurrence-only mutation fractions demonstrated that shared mutations, but not private mutations, showed positive dN/dS in all three glioma subtypes, indicating that only shared mutations (including truncal mutations) are likely subject to positive selection (Fig. 2c). The dN/dS ratio of initial-only mutations showed that these are neither positively nor negatively selected for, while recurrence-only mutations were subject to negative selection in IDHwt.

To verify the reduced selective pressure in the private mutations we used an orthogonal method to test for evidence of selection (neutralitytestR)[30]. The method uses variant allele frequency distributions and mutation rates to detect whether profiles significantly deviate from a model of neutral evolution (i.e. as depicted by a linear relationship in Fig. 2d). In accordance with dN/dS results, both initial-only and recurrence-only subclonal mutations demonstrated subclonal dynamics consistent with neutral evolution (Fig. 2d). While the distribution of mutation variant allele fractions shared between initial and recurrence were primarily clonal, we observed that shared subclonal mutations deviated from linearity and were consistent with selection both in non-hypermutators and hypermutators (Fig. 2d, Extended Data Fig. 6a-b), providing additional support that the strongest selective forces occur predominantly early in gliomagenesis.

Determining selection strength at the cohort-level may mask intertumoral and temporal heterogeneity that exists in individual evolutionary trajectories. To determine the strength of selection at each tumor time point we used a previously described Bayesian framework for determining selection in individual samples (i.e. SubClonalSelection) [15]. Briefly, the method simultaneously provides sample-specific probabilities for both selection and neutrality while modeling sources of noise in sequencing data. The classification of selection or neutral at each time point is determined by whichever model has the greater probability. Given the stringent requirements for the algorithm, 183 patients were included in this analysis with at least one time point, and 104 patients with both time points, quantified (16 IDHmutant-codels, 29 IDHmutant-noncodels, 59 IDHwt, Supplementary Table 3). Neutral to Neutral was the most common evolutionary trajectory across all three subtypes (52%), and IDHwt tumors displayed the highest observed selection at any time point with selection measured in 64% of tumors (Fisher's exact test $P = 0.01$, Fig. 2e, Supplementary Table 3). This classification of neutrality reflects the accumulation of random mutations that results in no or undetectable selection, but does not necessarily indicate a non-evolving tumor as current sequencing approaches are only able to

detect early expansion of subclonal cancer cell populations[30]. We found that IDHwt gliomas with evidence for selection at recurrence had a shorter overall survival than IDHwt gliomas with stronger evidence for neutrality at recurrence (P = 2.7E-02; log-rank statistic, Fig. 2f), suggesting that subclonal competition associates with more aggressive tumor behavior. To address the limitations of smaller sample sizes in the IDH-mutant subtypes, we performed a Cox proportional hazards model including age at first diagnosis, all three glioma subtypes, and mode of selection at recurrence. This analysis revealed that selection at recurrence was significantly associated with shorter survival across subtypes (HR = 1.53 95% CI 1.00-2.41, P = 4.8E-02, Supplementary Table 4). We next investigated whether radiation and chemotherapy, i.e. the commonly used therapies to treat glioma in adult patients after surgery, imposed a selective effect, by comparing the evolutionary trajectory as well as evolutionary status at recurrence with treatment and other clinical variables. We did not observe any significant associations between subclonal selection and radiation therapy or chemotherapy (Fisher's exact-test $P > 0.05$, Supplementary Table 5), indicating that standard therapeutic approaches for glioma may have relatively little impact on the subclonal architecture of the tumor. Together, our evolutionary and clonal analyses raise the possibility that the survival benefit derived from standard chemoradiation therapy results from a tumor cell elimination effect in which all cells are similarly susceptible, rather than selective killing of more sensitive glioma cells.

Patterns of glioma driver alteration frequencies over time

We next considered how the stability, acquisition, and loss of mutation and copy number drivers over time may shape glioma evolution[4]. Beyond determining patterns of global selection, the aforementioned dN/dScv method nominated 12 candidate mutation driver genes based on the local distribution of nonsynonymous and synonymous mutations ($Q < 0.05$, Fig. 3a, Extended Data Fig. 7a). Similarly, we used GISTIC to determine significant copy number alterations and recapitulated previously identified drivers (Extended Data Fig. 7b)[31]. Mutations in *IDH1* and chromosome arm level losses of 1p and 19q have been suggested as glioma-initiating events[14]. In line with that role, IDH mutations and chromosome 1p/19q codeletions were never lost or acquired during the surgical interval (Fig. 3a, Extended Data Fig. 8a). Similarly, we observed that detected *TERT* promoter mutations were almost exclusively shared throughout the IDHmutant-codel and IDHwt subtypes, though many samples lacked sufficient coverage in this GC-rich region. Chromosome 7 gains and chromosome 10 losses were present in a large majority of IDHwt initial tumors and persisted into recurrence. While many glioma-initiating alterations were stable during the life of a tumor, shifts in the fraction of cancer cells harboring an event may indicate a time dependency of drivers.

To determine the temporal order and the potential changes in cellular prevalence of the shared driver events we ordered events in each sample by their CCF (Extended Data Fig. 9). In the IDHmutant-codel subtype, chromosome 19q deletions and chromosome 1p deletions were not significantly different in the initial tumor (P = 0.41), but 19q deletions were significantly lower at recurrence (P = 0.04) suggesting a dilution of this event as some tumors progress. *ATRX* mutations in IDHmutant-noncodel initial tumors demonstrated lower CCFs compared with *TP53* (P = 0.03) and *IDH1* (P = 0.10) mutations, suggesting *IDH1* and *TP53* mutations precede *ATRX* inactivation[14]. ATRX plays a role in telomere maintenance and this process is likely to become active only after tumors have undergone a period of cellular crisis[14,32]. There was no difference in CCF between *IDH1* and *TP53* amongst initial gliomas (P = 0.98), *IDH1* mutations demonstrated significantly lower CCFs compared with *TP53* (P = 0.0018) in recurrent gliomas. Recent reports suggest that *IDH1* becomes dispensable once the initial tumor has fully formed[33], that the oncoprotein product of *IDH* mutations decreases in cultured cells[34] and the mutation sometimes disappears in recurrent human tumors[35]. While we did not find any evidence of the latter, our findings are generally in line what has been described, and suggest that mutant *IDH* may be less essential for tumor survival beyond its initiation. We did not observe any CCF differences among driver mutations detected in IDHwt tumors at either time point, however we found consistently higher CCFs for chromosome 10 deletions compared with chromosome 7 amplifications (i.e. 10p deletion CCF > 7p amplification CCF, P = 0.0036) implying that chromosome 10 deletions arise earlier and remain dominant in typical IDHwt development[36]. Similarly, there was no difference in CCF between *CDKN2A* deletion and *EGFR* amplification (P = 0.70), but we observed a modest difference between *EGFR* and chromosomal events (i.e. 10p del vs *EGFR* amp, P = 0.0019) despite no significant difference between *CDKN2A* deletion and chromosomal events (i.e. 10p del vs CDKN2A del, P = 0.33). The consistently high CCF for *EGFR* amplifications could indicate that these events precede even the larger chromosomal aberrations, or alternatively that high levels of extrachromosomal *EGFR* may artificially inflate CCF [37].

Individual drivers did not demonstrate any significant consistent changes between the initial tumor and recurrence (Extended Data Fig. 10a). Possibly these drivers follow general trends of the individual tumor over time despite remaining important throughout the course of disease. For example, when separated by subtype, *TP53* mutations showed an increase in CCF among IDHmut-noncodel tumors (P = 0.037) reflecting a decreased heterogeneity, whereas IDHwt *TP53* mutations tended to have decreased CCF values potentially reflecting increased tumor heterogeneity at recurrence, although this change was not statistically significant (P =

0.13, Extended Data Fig. 10b-c). We did not observe any differences in *IDH1* CCF over time among IDHmut-noncodel tumors, possibly because the general trend of these tumors to increase in CCF is counteracted by the biological loss of relevance of mutant *IDH1* over time. Indeed, a gross comparison of individual mutation CCFs amongst shared mutations demonstrated a slight increase amongst IDHmut-noncodel tumors ($P < 0.0001$) and a modest decrease in IDHwt tumors ($P < 0.0001$, Extended Data Fig. 10d). To ensure that these results were not biased due to unbalanced contribution of mutations from individual patients, we tested for CCF changes between initial tumor and recurrence in each patient. This analysis indicated a slight decrease in heterogeneity amongst IDHmut-noncodel tumors and an increase in heterogeneity in IDHwt tumors (Extended Data Fig. 10e).

We investigated somatic alteration acquisitions or losses over time. Again, we found a paucity of consistent change in recurrent tumors despite the characteristic landscape of these tumors at first presentation. While gene-specific enrichment of many recurrence-only mutations were found in hypermutated tumors, there was no enrichment for somatic gene alterations in non-hypermutators, suggesting a lack of pan-glioma pathways driving recurrence (Extended Data Fig. 8b). Within subtypes we detected an enrichment in *CDKN2A* homozygous deletions (Fig. 3a, Extended Data Fig. 8a) in recurrent IDHmutant-noncodels, which was corroborated by additional cell cycle gene alterations (focal gain of *CCND2, CDK4*, *CDK6*, mutation or homozygous loss of *RB1*). Mutations in cell cycle checkpoint control genes are associated with genomic instability [38]. Therefore, we analyzed the levels of aneuploidy in our cohort by measuring the proportion of the genome that had undergone aneuploidy events as well as counting aneuploid chromosome arms per tumor using a previously described method (Extended Data Fig. 11a-b)[39]. We observed that IDHmutant-noncodel tumors had a higher level of aneuploidy at recurrence (Wilcoxon rank sum test $P = 1.4E-06$ total aneuploidy, $p = 8.6E-03$ arm-level aneuploidy, Extended Data Fig. 11c-d) with tumors carrying acquired cell cycle gene alterations displaying the largest increases in aneuploidy ($P = 7.6E-06$; Wilcoxon rank sum test, Fig. 3b). We reasoned that *CDKN2A* deletions may precede aneuploidy. Homozygous *CDKN2A* deletions had significantly higher CCFs compared to average CNV CCF across the genome (as a surrogate for aneuploidy related copy number changes), suggesting that *CDKN2A* loss preceded aneuploidy (Fig. 3c). These alterations may hasten disease progression as patients with either cell cycle alterations or the largest increases in aneuploidy at recurrence demonstrated significantly shorter survival than patients without these alterations (log-rank test $P < 0.0001$, Fig. 3d). Taken together, the driver gene patterns are consistent with a continued

dependence during recurrence and implies that therapy does not result in selection of specific sets of molecular changes.

Neoantigen selection is stable throughout tumor progression. Immunoediting is the principle that the immune system prunes tumor cells carrying immunogenic (neo-)antigens, resulting in the selection of subclones capable of evading the immune response. Evidence of this process has been shown in several cancer types, including glioma [40-43], and suggests active immunosurveillance that may be therapeutically exploited [44]. To determine the extent to which this process was taking place in our cohort, we computationally predicted neoantigen-generating mutations using a previously developed pipeline [45]. For this analysis, we defined a neoantigen-causing mutation as any exonic mutation giving rise to an 8-11mer peptide that bound a patient's HLA class I proteins at a binding affinity score (IC50) less than 500nM and equal or better than the wild-type form of the peptide[45]. As expected, the neoantigen burden across the GLASS cohort was strongly correlated with exonic mutation load (Spearman's Rho = 0.89), with 43% of nonsynonymous exonic mutations giving rise to neoantigens on average. This number did not significantly differ by tumor subtype or between initial and recurrent tumor pairs (Fig. 4a), suggesting stable neoantigen formation rates throughout glioma. The most common neoantigen we identified in our cohort was KPIIIGHHAY, which arose from the clonal R132H mutation in *IDH1* and was present in the initial and recurrent tumors of 22 out of 88 IDH-mutant patients. Beyond mutations in *IDH1*, no mutations gave rise to a neoantigen found in more than three tumors at a given timepoint (Supplementary Table 6). When examining how the cancer cell fractions of neoantigens changed between initial and recurrent tumors, we did not observe any differences compared with non-immunogenic mutations, suggesting a lack of immunologic selection at a cohort-level (Extended Data Fig. 12).

We next examined the extent to which immunoediting occurred in specific samples by applying a published method that compares each sample's observed neoantigen rates to their empirically-derived expected rates[43]. The output of this method produces a score where values < 1 indicate a depletion in neoantigens that is suggestive of immunoediting during a tumor's development. None of the three subtypes exhibited significant levels of depletion, though IDHwt tumors did exhibit significantly lower scores compared with those from IDHmut-noncodels (Wilcoxon rank-sum test, $P = 0.02$; Fig. 4b). There was additionally no association between neoantigen depletion and survival when adjusting for subtype and age (Wald test, $P > 0.05$), nor did we observe a difference between samples with neutral evolution dynamics compared to those exhibiting evidence of subclonal selection. Notably, the observed-to-expected neoantigen rate was significantly associated with the total number of unique HLA loci in a patient

(Spearman's Rho = 0.28, P = 5.0E-10), reflecting similar findings in lung cancer [46]. This may bias associations detected across patients, thus we focused our remaining analyses within samples over time. When comparing samples longitudinally, we found that the observed to expected neoantigen ratio was strongly correlated between initial and recurrent tumors (Pearson's R = 0.72, P = 2E-35), suggesting a constant rate of immunosurveillance in a patient over time (Fig. 4c). Hypermutators have previously been associated with elevated levels of cytolytic cells that may select against neoantigen-bearing cells during evolution [42]. However, we did not observe any differences in neoantigen depletion between hypermutated recurrent tumors and their initial counterparts, nor did we observe differences between hypermutated and non-hypermutated recurrent tumors, indicating that immunoediting activity is not related to the total number of mutations in a sample (Wilcoxon rank-sum test P > 0.05; Extend Data Fig. 12). While we did not observe differences between a patient's initial and recurrent tumors, we reasoned that immunoediting may take place at variable rates throughout a tumor's evolution. Thus, we calculated an observed-to-expected neoantigen ratio for each patient's set of clonal mutations, which likely arose earlier in tumor evolution, and their subclonal mutations, which likely arose later. We did not observe a significant difference in the observed-to-expected neoantigen ratio of each patient's clonal and subclonal neoantigens, regardless of glioma subtype or whether the sample was an initial tumor or recurrence (Wilcoxon rank-sum test P > 0.05; Fig. 4d). Overall, these analyses suggested that the rates of immunosurveillance are stable in the window between tumor initiation and diagnosis, as well as the interval between diagnosis and resection of the recurrent tumor.

While our neoantigen depletion analyses revealed high levels of stability throughout a tumor's life, we were unable to identify glioma-intrinsic factors that explained differences between samples. To determine whether there were immunologic factors associated with neoantigen depletion, we analyzed CIBERSORT relative immune cell fractions from a subset of samples that had undergone expression profiling in a previous study (n = 84 from 42 tumor pairs) [42,47]. Within initial tumors we did not observe any significant differences in cellular abundance between depleted (ratio < 1) and non-depleted samples (ratio > 1), however in recurrent tumors, samples with an observed-to-expected neoantigen ratio > 1 exhibited significantly higher levels of macrophages and neutrophils (Wilcoxon rank-sum test P < 0.05; Extended Data Fig. 12c). These results suggest that the immunoediting activity in a given patient may be driven by the presence of specific myeloid cells in their tumor, though a larger cohort of samples with expression data will be needed to validate this finding.

DISCUSSION

We reconstructed the evolutionary trajectories of 222 patients with glioma to better understand treatment failures and tumor progression. Our collective analyses show that each glioma follows a unique path toward recurrence with few common changes shared between patients. Among the recurrence-specific features, we report that hypermutation following treatment with an alkylating agent occurs in all glioma subtypes. Notably, hypermutation did not confer a detrimental effect on survival raising question whether the associated malignant transformation is a cause versus a consequence. We found that gliomas harboring an IDH mutation without 1p/19q-codeletion often acquire cell cycle alterations and aneuploidy as they progress over time, and these changes were associated with decreased survival. Nevertheless, the majority of tumors, despite similarities in their treatment, did not show common features as they evolved suggesting that post-treatment glioma evolution is heavily shaped by genetic drift.

Alkylating agent-associated hypermutation has been previously studied in glioma, yet its clinical significance remains uncertain[18-21,24]. Our results provide evidence that acquisition of a hypermutator phenotype did not drive progression as supported by a lack of association with survival and the finding that mutations derived from the hypermutation process were subclonal in half of the hypermutators. Future analyses based on larger cohorts are needed to explore whether there is an association with the number of alkylating agent cycles used, *MGMT* DNA methylation status, and whether hypermutators respond better to specific therapies (e.g., immunotherapy). Separately, an increase in cell cycle alterations in recurrent IDHmutant-noncodels was previously shown to converge with a loss of DNA methylation phenotype and elevated activity of cycling cell gene expression programs[4,48]. Worse outcomes for IDHmutant-noncodel patients with either cell cycle alterations or increases in aneuploidy provide rationale to therapeutically target these more aggressive phenotypes with compounds that disrupt microtubule dynamics[49] or CDK inhibitors[50]. Monitoring these critical events in glioma evolution through liquid biopsies may potentially help track and even delay these drivers of tumor recurrence [51].

Our results provide evidence that standard treatments did not coerce the glioma genome down predictable paths. Nevertheless, recurrent tumors that displayed evidence of recent subclonal selection had significantly reduced survival independent of other prognostic factors suggesting that selection was associated with more aggressive tumors. Neutral evolution was the primary evolutionary mode detected in both initial and recurrent glioma, which may in part be due to our ability to detect clonal selection with the available data[23]. Deep whole-genome sequencing datasets are best suited for these analyses and may become available in the future,

via GLASS or otherwise. Similarly, we did not observe a difference in the rate of neoantigen depletion between initial and recurrent disease. While the levels of immunoediting remained constant, additional molecular and immonological data will be needed to fully understand the impact immunoediting variability across tumors has on glioma evolution[16]. We found that clonal neoantigens arising from the *IDH1* R132H mutation persisted from the initial tumor into the recurrence, justifying neoantigen vaccine approaches as treatments for primary and recurrent glioma[52,53]. Going forward, these findings help shape our perspective on what constitutes an optimal treatment, and what approaches would result in the greatest removal or killing of glioma cells possible.

Genomic characterization efforts such as TCGA have greatly increased our understanding of glioma biology, but were limited to a single snapshot in evolutionary time. The Glioma Longitudinal Analysis Consortium was initiated in recognition of the observation that creating a longitudinal molecular catalogue demands a community effort, and that such a resource may enable critical new insights into glioma evolution. This resource can be utilized by the research community: to determine markers of response, to identify evolutionary bottlenecks and to show that treatment can impact mode of tumor evolution. Future development of GLASS including methods that aim to characterize tumors at epigenetic, gene expression, imaging, and single-cell levels are needed to comprehensively describe this process. In summary, our production and analysis of the GLASS resource provides a framework to study the most frequent patterns of glioma evolution.

ACKNOWLEDGEMENTS

This work is dedicated to the memory of Simone Bischoff-Lardenoije and is made possible by the patients and their families whom generously contributed to this study. This work is supported by the National Brain Tumor Society, Oligo Research Fund; Cancer Center Support grants P30CA16672 and P30CA034196; Cancer Prevention & Research Institute of Texas (CPRIT) grant number R140606; Agilent Technologies (R.G.W.V.); the National Institutes of Health-National Cancer institute for the following grants: NCI CA170278 (L.M.P., M.M.T., N.H.), NCI R01CA222146 (L.M.P, N.H.), NCI R01CA230031 (J.H.C., J.N.), NCI R01CA188288 (J.S.B., R.B., P.B., K.L.L., A.C., A.E.S.), R01CA179044 (Antonio Iavarone), U54CA193313 (Antonio Iavarone). The National Brain Tumor Society (W.K.A.Y.; J.D.G). Brain Tumour Northwest tissue bank (including the Walton research tissue bank) is supported by the Sidney Driscol Neuroscience Foundation and part of the Walton Centre and Lancashire Teaching Hospitals NHS Foundation Trusts (A.B., M.D.J.). Support is also provided by a Leeds Charitable

Foundation grant (9R11/14-11 to LFS), University of Leeds Academic Fellowship (11001061) (L.F.S.) and Studentship (11061191) (G.T.) as well as Leeds Teaching Hospitals NHS Trust (Aruna Chakravarti, Azzam Ismail). The Leeds Multidisciplinary Research Tissue Bank staff was funded by the PPR Foundation and The University of Leeds (S.C.S.). C.W. is funded by The Brain Tumour Charity (Grants 10/136 & GN-000580). G.T. is funded by EKFS 2015_Kolleg_14. R01CA218144 (P.S.L, E.J.C, J.C. A.K.L.) and Strain for the Brain, Milwaukee, WI (P.S.L, E.J.C, J.C. A.K.L.). E.K is recipient of an MD-Fellowship by the Boehringer Ingelheim Fonds and is supported by the German National Academic Foundation. The Leeds Multidisciplinary Research Tissue Bank staff was funded by the PPR Foundation and part of the University of Leeds (S.C.S.). GLASS-Austria was funded by the Austrian Science Fund project KLI394 (A.W.). GLASS-Germany was funded by the German Ministry of Education and Research (BMBF) 031A425 (G.R., P.L.) and German Cancer Aid (DKH) 70-3163-Wi 3 (M.W.). GLASS-NL receives support from KWF/Dutch Cancer Society project11026 (MCMK, PW, RGWV, PJF, JMN, MS, BAW). We thank the University of Colorado Denver Central Nervous System Biorepository (D.R.O.) for providing tissue samples. Sponsoring was also received from the National Institute of Neurological Disorders and Stroke (NINDS R01NS094615, R.G.), the Brain Tumour Charity (grant 10/136, C.W.), National Health and Medical Research Council project grant (A.M.D.). F.P.B. is supported by the JAX Scholar program and the National Cancer Institute (K99 CA226387); K.C.J. is the recipient of an American Cancer Society Fellowship (130984-PF-17-141-01-DMC). We thank the Jackson Laboratory Clinical and Translation Support team for coordinating all data transfer agreements. We thank Matt Wimsatt for assistance in graphic design.

CONFLICTS OF INTEREST

R.G.W.V. declares equity in Pretzel Therapeutics. M.K. receives research grants from BMS and ABBVie. P.K.B. is a consultant for Lilly, Genentech-Roche, Angiochem and Tesaro. P.K.B. receives institutional funding from Merck and Pfizer and honoraria from Merch and Genentech-Roche. W.K.A.Y serves in a consulting or advisory role at DNAtrix Therapeutics. M.W. receives funding from Acceleron, Actelion, Bayer, Isarna, Merck, Sharp & Dohme, Merck (EMD, Darmstadt), Novocure, OGD2, Pigur and Roche as well as honoraria from BMS, Celldex, Immunocellular Therapeutics, Isarna, Magforce, Merck, Sharp & Dohme, Merck (EMD, Darmstadt), Northwest Biotherapeutics, Novocure, Pfizer, Roche, Teva and Tocagen. G.R. receives funding from Roche and Merck (EMD, Darmstadt) as well as honoraria from AbbVie. M.S. is a central reviewer for Parexel Ltd and honoraria are paid to the institution. G.T. reports personal fees from Bristol-Myers-Squibb, personal fees from AbbVie, personal fees from

Novocure, personal fees from Medac, travel grants from Bristol-Myers-Squibb, education grants from Novocure, research grants from Roche Diagnostics, research grants from Medac, membership in the National Steering board of the TIGER NIS (Novocure) and the International Steering board of the ON-TRK NIS (Bayer).

CONTRIBUTIONS

D.M.A., D.A., P.B., J.S.B., R.B., C.B., P.K.B., D.J.B., A.B., A.C., E.J.C., J.C., G.F., M.N.F., Antonio I., M.D.J., M.K., P.S.L., M.L., P.L., K.L.L., T.M.M., A.M.M., D.N., N.N., H.N., C.Y.N., S.P.N., Houtan N., D.R.O., C.P., L.M.P., G.R., B.R., J.K.S., S.C.S., A.E.S., M.S., L.F.S., H.S., E.G.V.M., C.W., M.W., G.W., A.W., contributed to sample acquisition and processing, sequencing data coordination was performed by H.K, F.P.B and K.C.J., and clinical data coordination by A.D.M., and O.A.. Data analysis was led by F.P.B. and K.C.J. in collaboration with S.B.A., P.B., B.C., J.H.C., H.K., E.K, T.M.M., H.N., J.N., M.S., L.F.S., G.T., F.V. and R.G.W.V.. Clinical analysis was performed by A.D.M., L.M.P., and C.W.. Pathology review was completed, in part, by Aruna Chakrabarty, J.T.H., Azzam Ismail., and A.W.. F.P.B., K.C.J., A.D.M., F.V., and R.G.W.V. wrote the manuscript. K.D.A. and J.F.D. took charge in coordinating GLASS-MDACC; L.F.S. was the lead coordinator of the GLASS-Leeds cohort and B.A.W. of GLASS-Netherlands. R.G.W.V was the project lead and coordinator. Funding for the project was received by K.D.A., E.B.C., H.G., J.T.H., S.C.S., L.F.S.. All co-authors discussed the results and commented on the manuscript and Supplementary Information.

Methods

Data reporting No statistical methods were used to predetermine sample size.

DNA sequencing and data collection The GLASS dataset consists of both unpublished and published sequencing data as outlined in Supplementary Table 1. Among the cohort were exomes from 436 glioma samples (200 patients), whole-genome from 165 glioma samples (78 patients), with overlapping exome/whole-genome data on 78 glioma samples (38 patients). A matching germline sequence was available for all patients. The dataset includes 257 sets of at least two time-separated tumor samples, seventeen standalone recurrences, and 19 patients with at least two geographically distinct tumor portions. More specifically, the dataset includes exome or whole-genome sequencing data on 211 primary gliomas, 234 first recurrences, 32 second recurrences, 11 third recurrences and one fourth recurrence (Supplementary Table 7).

Newly generated whole genome sequencing data for the Chinese University of Hong Kong (HK), Northern Sydney Cancer Centre (NS) and MD Anderson Cancer Center (MD) cohorts were subjected to 150 base paired-end sequencing. The HK samples were sequenced using a HiSeqX while the NS and MD cohorts were sequenced using a NovaSeq according to Illumina's

protocols. Whole exome capture was performed using the following platforms as reported in previous publications. Agilent SureSelect Human All Exon 50Mb capture kit was used for patients SF-0001- SF-0021, Agilent SureSelect Human All Exon V4 capture kit was used for patients SF-0024 – SF-0029 in the UC San Francisco cohort. Agilent SureSelect Human All Exon v4 or v5 was used to capture samples in the Kyoto University cohort. Samsung Medical Center cohort reported using Agilent SureSelect kit for patients SM-R056 – SM-R071, SM-R075, SM-R076, SM-R095- SM-R114 while Illumina TruSeq Exome-capture kit was used for patient SM-R072. Exome capture was performed using Agilent SureSelect Human All Exon 50 Mb in The Cancer Genome Atlas (TCGA)-GBM cohort and Agilent SureSelect Human All Exon v2.0, 44Mb kit in the TCGA-LGG cohort. Columbia University cases were captured using Agilent V3 50M kit, sequencing 90bp PE for samples R009-TP, R009R1, R011TP, R011R1, R014TP, R014R1, R017-R1, R018-R1, R019-R1. Mapping files of initial tumor and normal samples of patients R017 – R019 were obtained from TCGA through CG-hub. All other samples were captured using Agilent SureSelect XT Human All Exon v4 Kit, PE, 80M reads, 150X on target coverage. Samples in the Henry Ford Hospital cohort were multiplexed and sequenced using Illumina HiSeq 2000 by the Sequencing and Microarray Facility at an average target exome coverage of 100× using 76-bp paired-end reads. Samples in the HK cohort were subjected to 75 base paired-end sequencing for HK-0001 – HK-0004 as performed NextSeq in high output mode. In the Leeds Cohort (LU) SureSelectXT V5 kit (PE100) was used to construct exome libraries. Illumina TruSeq Exome capture kit was used for samples at the Medical University of Vienna – CeMM.

GLASS identifiers A GLASS barcode system was created, based on TCGA barcode design, in an effort to de-identify patient information and provide an organized framework for the different pieces of the dataset.

GLASS barcodes are composed of 24 characters. The first four characters specify the project (either GLSS or TCGA). All datasets submitted to the GLASS consortium, published and unpublished, were given the GLSS project ID. Samples that were part of the TCGA cohorts (TCGA GBM and TCGA LGG) were given a TCGA designation. The next two characters designate the center where the samples were either acquired or sequenced (Supplementary Table 7). This is followed by the four-character center specific patient identification that was kept as close as possible to the patient identification provided by the collaborators to allow a simplified trace back process. Patient data is divided by a relative sample type, such as initial tumor (TP), recurrent tumor (R1), normal tissue (NB, NM, etc), or metastatic tumor sample (M1). If there was more than one recurrence the relative number was specified following “R”. Some patients had surgeries for which a biospecimen was unavailable. Thus, a surgical number was also provided to indicate temporal ordering (Supplementary Table 8). To include spatially separated samples the portion designation was added, which is followed by one character specifying the type of analyte, either DNA (D) or RNA (R). As there is variation in the sequencing analysis, a three-character designation represents either whole genome (WGS) or whole exome sequencing (WXS). The last part of the GLASS barcode is a six-character designation unique to each barcode that was randomly generated.

Computational pipelines All pipelines were developed using snakemake 5.2.2 [54]. Unless otherwise stated, all tools mentioned are part of the GATK 4 suite [55]. All data was collected at a

central location (The Jackson Laboratory) and was analyzed using homogenous pipelines capable of processing both raw fastq files as well as re-process previously analyzed bam files.

Alignment and pre-processing Data pre-processing was conducted in accordance to the GATK Best Practices using GATK 4.0.10.1. Briefly, aligned BAM files were separated by read group, sanitized and stripped of alignments and attributes using ‘RevertSam’, giving one unaligned BAM (uBAM) file per readgroup. Uniform readgroups were assigned to uBAM files using ‘AddOrReplaceReadgroups’. Similarly, unaligned fastq files were assigned uniformly designated readgroup attributes and converted to uBAM format using 'FastqToSam'. uBAM files underwent quality control using 'FastQC 0.11.7'. Sequencing adapters were marked using ‘MarkIlluminaAdapters’. uBAM files were finally reverted to interleaved fastq format using ‘SamToFastq’, aligned to the b37 genome ('human_g1k_v37_decoy') using 'BWA MEM 0.7.17', attributes were restored using 'MergeBamAlignment'. 'MarkDuplicates' was then used to merge aligned BAM files from multiple readgroups and to mark PCR and optical duplicates across identical sequencing libraries. Lastly, base recalibration was performed using 'BaseRecalibrator' followed by 'ApplyBQSR'. Coverage statistics were gathered using 'CollectWgsMetrics'. Alignment QC was performed running 'ValidateSamFile' on the final BAM file and QC results were inspected using 'MultiQC 1.6a0' [56]. A haplotype database for fingerprinting was generated using a modified version of the code on https://github.com/naumanjaved/fingerprint_maps. The tool ‘CrosscheckFingerprints’ was used to confirm that all readgroups within a sample belong to the same individual, and that all samples from one individual match. Any mismatches were marked and excluded from further analysis.

Variant detection Variant detection was performed in accordance to the GATK Best practices using GATK 4.1.0.0. Germline variants were called from control samples using Mutect2 in artifact detection mode and pooled into a cohort-wide panel of normals. Somatic variants were subsequently called in individual tumor samples (single-sample mode) and in entire patients using GATK 4.1 Mutect2 in multi-sample mode. Mutect2 was given matched control samples, the aforementioned panel of normals and the gnomAD germline resource as additional controls. Cross-sample contamination was evaluated using ‘GetPileupSummaries’ and ‘CalculateContamination’ run for both tumor and matching control samples. Read orientation artifacts were evaluated using ‘CollectF1R2Counts’ and ‘LearnReadOrientationModel’. Somatic likelihood, read orientation, sequence context, germline and contamination filters were applied using ‘FilterMutectCalls’.

Variant post-processing BCFTools 1.9 was used to normalize, sort and index variants[57]. A consensus VCF was generated from all variants in the cohort, removing any duplicate variants. The consensus VCF file was annotated using GATK 4.1 Funcotator and the v1.6.20190124s annotation data source. Allele frequencies (AFs) from multi-sample Mutect2 were used to compare AFs between related samples. Multi-sample Mutect2 calls and filters mutations across a patient as a whole and does not determine mutation calls in a single samples. Single-sample mutation calls were overlaid on the multi-sample calls to infer whether variants were called in individual samples. Single-sample called variants that were not present in the multi-sample callset were discarded.

Mutational rates Mutational rates were calculated as the number of mutations per megabase (Mb) sequenced. A minimum coverage threshold of 15x was required for each base. DNA

hypermutation was defined for recurrent tumors with greater than 10 mutations per Mb sequenced as these values were considered outliers (1.5 times the interquartile range above the upper quartile). Notably, there were a few initial gliomas that demonstrated a mutational frequency above 10 mutations per Mb. However, the “hypermutation” classification was restricted to only patients with this level at recurrence since these likely reflect different evolutionary paths.

Mutational signatures The relative contributions of the COSMIC mutational signatures were determined from a patient’s initial-only, recurrence-only, and shared mutations by solving the non-negative-least squares (NNLS) problem for each set of mutations using the 30 signatures from version 2 (March 2015). Six signatures were dominantly enriched in at least 3% of the fractions and we resolved the NNLS using the reduced six-signature model to increase accuracy and reduce noise.

Copy number segmentation Copy number identification was performed according to the GATK Best Practices and is outlined briefly here. The pipeline differs slightly for whole genomes and whole exomes. For genomes, the genome was segmented into 10kb bins using ‘PreprocessIntervals’. For exomes, overlapping regions between several commonly used capture kits (Broad Human Exome b37, Nextera Rapid Capture, TruSeq Exome, SeqCap EZ Exome V3, Agilent SureSelect V4, Agilent SureSelect V7) were identified using ‘bedtools multiIntersectBed’. The tool ‘PreprocessIntervals’ was used to apply 1kb padding and to merge overlapping intervals. In parallel, ‘SelectVariants’ was used to subset the gnomAD resource of germline variants to variants with a population AF greater than 5%. Next, ‘CollectReadcounts’ was used to count reads in the bins generated by ‘PreprocessIntervals’ separately for autosomes and allosomes. In parallel, ‘CollectAllelicCounts’ was used to count reference and alternate reads at gnomAD variant sites with a population AF greater than 5%. The cohort was subsequently split into batches determined by sequencing center and ‘CreateReadCountPanelOfNormals’ was used to create a panel of normal (PON) for each batch. PONs were created separately for allosomes and autosomes, and allosomes were separated further by sex. To further improve the panel of normals, GC content annotation of each interval as determined by ‘AnnotateIntervals’ were given. Next, ‘DenoiseReadCounts’ was used to denoise the binned readcounts output by ‘CollectReadCounts’, given a PON determined by batch, chromosomes (allosomes or autosomes) and sex. Denoised copy ratios were plotted and inspected for quality concerns using ‘PlotDenoisedCopyRatios’. The tool ‘ModelSegments’ is an implementation of a gaussian-kernel binary-segmentation algorithm and was used to merge contiguous segments and assign copy and allelic ratios. The results of this segmentation were plotted using ‘PlotModeledSegments’ and inspected for quality concerns.

Copy number calling A copy number caller loosely based on GATK ‘CallCopyRatioSegments’ (which in turn is based off of ReCapSeg) and GISTIC was implemented to call both arm-level and high-level copy number changes, respectively[31,58].

Segments (from ‘ModelSegments’) with a non-log2 copy ratio between 0.9 and 1.1 were determined to be neutral. These segments were then weighted by length and a weighted mean and standard deviation (sd) non-log2 copy ratio (once-filtered) were determined again. Outlier segments are removed and once again a weighted mean and sd non-log2 copy ratio (twice-filtered) were determined. Segments with a non-log2 copy ratio between 0.9 and 1.1 and

segments within two standard deviations of the twice-filtered mean were determined to be neutral, and segments outside of these boundaries were determined to have a low-level amplification or deletion, depending on the direction.

The weighted mean and sd of the non-log2 copy ratio (once-filtered) was then determined individually for each chromosome arm. Outlier segments were removed and the weighted mean and sd of the non-log2 copy ratio (twice-filtered) was determined again. In order to determine a high-level amplification and deletion threshold, the most highly amplified and deleted chromosome arms were selected, respectively. The twice-filtered mean plus (high level amplification) or minus (high level deletion) two times the sd of the selected arms were used as high-level thresholds.

Gene level copy number were called by intersecting the gene boundaries with the segment intervals and by calculating the weighted non-log2 copy ratio for that gene. The copy number call for that gene was then determined by comparing the gene-level non-log2 copy ratio to the previously determined thresholds.

dNdScv The R package dNdScv[59] (https://github.com/im3sanger/dndscv) was run using the default and recommended parameters for all mutations in initial tumor samples, recurrent tumor samples, and for each mutational fraction (unique to initial, unique to recurrent and shared). All analyses were conducted separately within the three main tumor subtypes.

Aneuploidy calculation The most reductive metric of aneuploidy was computed by taking the size of all non-neutral segments divided by the size of all segments. The resulting aneuploidy value indicates the proportion of the segmented genome that is non-diploid.

In parallel, an arm-level aneuploidy score modeled after a previously described method was computed[39]. Briefly, adjacent segments with identical arm-level calls (-1, 0 or 1) were merged into a single segment with a single call. For each merged/reduced segment, the proportion of the chromosome arm it spans was calculated. Segments spanning greater than 80% of the arm length resulted in a call of either -1 (loss), 0 (neutral) or +1 (gain) to the entire arm, or NA if no contiguous segment spanned at least 80% of the arm's length. For each sample the number of arms with a non-neutral event was finally counted. The resulting aneuploidy score is a positive integer with a minimum value of 0 (no chromosomal arm-level events detected) and a maximum value of 39 (total number of autosomal chromosome arms excluding the short arms for chromosomes 13, 14, 15, 21, and 22).

Estimates of evolutionary pressures Evolutionary pressures were evaluated both by variant status and glioma subtype using the neutralitytestr algorithm as previously described (R-package: neutralitytestr version: 0.0.2, https://github.com/marcjwilliams1/neutralitytestr)[30]. Individual variant allele frequency vectors were merged at the level of glioma subtype by variant status. Only mutations found in copy-neutral regions should were included in these analyses. For all else, default parameters were used. Merged VAF distributions were deemed to be selected when the neutral null hypothesis was rejected using several metrics. Tests for neutrality required that both R^2 values < 0.98 and the area between the two curves of 1) merged VAF data and 2) a normalized distribution expected under neutrality to be significantly different.

The SubclonalSelection algorithm was applied to GLASS mutation data to measure the selection strength in individual tumor samples (Julia package: SubclonalSelection, https://github.com/marcjwilliams1/SubClonalSelection.jl)[15]. Patients that had samples at both

timepoints with a TITAN-defined purity estimate >= 0.5 and >= 25 subclonal mutations in non-diploid regions were included. Mean coverage across all mutations was used as the "read_depth" input parameter and the model was run with the recommended 10^6 iterations and 1000 particles. Samples were classified as neutral or selected based on the model that had the highest probability, in line with the prior applications to TCGA data[15]. Classification based on the highest model probability yielded stable results there was not a significant change in proportions when setting a higher classification probability threshold ($P > 0.05$, Pearson's Chi-square test, for both probability thresholds of 0.6 and 0.7). At all three probability thresholds (0.5, 0.6, and 0.7), Kaplan-Meier survival analyses between selection at recurrence and overall survival continued to indicate that patients with IDHwt tumors that were selected had a worse overall survival ($P = 0.03$ (n=81), $P = 0.01$ (n=66), $P = 0.01$ (n=56) respectively).

Mutation clonality Each patient's clonal architecture was inferred using PyClone (version 0.13.1) by grouping SNVs into clonal clusters (https://github.com/aroth85/pyclone). The patient-level input mutation matrix was reduced by limiting to sites with at least 30x coverage across all samples. PyClone was subsequently ran using a binomial density model, connected initiation, and 10000 iterations. Sample purities were provided for each patient and parental copy number (minor and major allele counts) from TITAN were given. PyClone results were post-processed using a burnin of 1000, thin of 1, minimum cluster size of 2 and a maximum number of clusters per patient of 12. Individual mutations were determined to be clonal if the PyClone cancer cell fraction (CCF) values were >= 0.5, subclonal for mutations with CCF >= 0.1 and CCF <0.5, mutations were considered non-clonal when CCF < 0.1 as previously described [60].

CNV clonality Allele specific copy number, tumor purity and ploidy estimates were derived using a probabilistic model (TITAN, version 1.19.1) for both whole genome and whole exome sequencing samples [27]. TITAN was supplied with the tumor denoised readcounts output by GATK DenoiseReadCounts and the tumor allelic counts at loci found to be heterozygous in control samples output by ModelSegments. An 'alphaK' (and 'alphaKHigh') parameter of 2500 and 10000 was used for exomes and genomes, respectively. The patient sex was provided in order to improve fitting allosomes. For each tumor-control pair TITAN was ran assuming an initial ploidy of two or three, and assuming 1 to 3 clusters, resulting in a total of six possible solutions per tumor/control pair. To select the optimal solution, TITAN's internal selectSolution function was used with a threshold of 0.15 giving additional weight to diploid solutions.

Timing analysis The CCF values output by TITAN or PyClone were used for separately timing copy number changes or mutations. To time specific copy number changes in genes, the average CCF for that gene was calculated. When timing mutations in genes, the highest CCF amongst the non-synonymous mutations was taken.

Neoantigen analyses Neoantigens in this analysis were defined as all 8-11-mer peptides that arose from an exonic nonsynonymous SNV or indel and bound their respective patient's HLA class I molecules at a binding affinity score (IC50) that was ≤ 500 nM and better than or equal to the wild-type form of the peptide. Each patient's 4-digit HLA class I types were inferred using OptiType (version 1.3.1, https://github.com/FRED-2/OptiType) run on each patient's matched normal sample[61]. VCF files for each tumor sample were annotated using Variant Effect Predictor (ensembl) with the Downstream and Wildtype plugins. Neoantigens from these VCFs were then called using pVACseq (version 4.0.10, https://github.com/griffithlab/pVAC-Seq)[45] run using

netMHCpan (version 2.8, http://www.cbs.dtu.dk/services/NetMHCpan-2.8/)[62]. For each pVACseq run, epitope length was set to 8, 9, 10, or 11, minimum binding affinity fold-change was set to 1, and downstream sequence length was set to full, with default parameters used for all other settings.

Downstream neoantigen analyses were performed using the pVACseq output linked to its respective mutation information. Neoantigen-causing mutations were defined as all mutations that gave rise to at least one neoantigen. Neoantigen depletion was calculated using a previously developed approach that compares each tumor's observed neoantigen rate to an empirically derived expected rate that assumes no selection against neoantigen-causing mutations[43]: From the gold set samples in the GLASS cohort (n = 222), define $\bar{N}_s$ to be the expected number of nonsynonymous missense SNVs per synonymous SNV with trinucleotide context s. $\bar{B}_s$ is then defined as the expected number of neoantigen-generating missense SNVs per nonsynonymous missense SNV with trinucleotide context s. For a given sample i, define Y_i as the sample's set of synonymous SNVs and $s(m)$ to be a synonymous SNV with trinucleotide context m. The expected number of nonsynonymous missense SNVs, N_{pred}, and neoantigen-causing mutations, B_{pred}, can then be calculated as follows:

$$N_{pred,i} = \sum_{m}^{Y_i} \bar{N}_{s(m)}$$

$$B_{pred,i} = \sum_{m}^{Y_i} \bar{N}_{s(m)} \bar{B}_{s(m)}$$

To obtain sample i's final neoantigen depletion ratio R_i, the observed number of neoantigen-causing mutations in the sample, $B_{obs,i}$ is divided by the sample's observed number of nonsynonymous missense SNVs, $N_{obs,i}$, and then this ratio is divided by the ratio of $B_{pred,i}$ and $N_{pred,i}$. Thus:

$$R_i = \frac{B_{obs,i}/N_{obs,i}}{B_{pred,i}/N_{pred,i}}$$

For analyses examining clonal/subclonal neoantigen depletion rates and fractional neoantigen depletion rates, the expected and observed numbers were calculated by subsetting a sample's SNVs by the respective criteria and then recalculating the ratio as described above. To mitigate overfitting, all analyses presented here utilized samples from patients with at least 3 neoantigen-causing mutations in their primary and recurrent tumors.

Immune cell analyses CIBERSORT relative immune cell fraction data used in downstream neoantigen analyses were downloaded from a previous publication[42].

Statistical methods All data analyses were conducted in R 3.4.2, Python 2.7.15, PostgreSQL 10.5, and Julia 0.7. All survival analyses including Kaplan-Meier plots and Cox proportional hazards models were conducted using the R packages survival and survminer.

Data availability All deidentified, non-protected access somatic variant profiles and clinical data are accessible via Synapse (http://synapse.org/glass). Raw data of the various sequencing datasets can be obtained per the overview provided in the Supplement.

Code availability All custom scripts and pipelines are available on the project's github page (https://github.com/TheJacksonLaboratory/GLASS).

References

1 Bettegowda, C. *et al.* Mutations in CIC and FUBP1 contribute to human oligodendroglioma. *Science* **333**, 1453-1455, doi:10.1126/science.1210557 (2011).

2 Brennan, C. W. *et al.* The somatic genomic landscape of glioblastoma. *Cell* **155**, 462-477, doi:10.1016/j.cell.2013.09.034 (2013).

3 Cancer Genome Atlas Research, N. Comprehensive genomic characterization defines human glioblastoma genes and core pathways. *Nature* **455**, 1061-1068, doi:10.1038/nature07385 (2008).

4 Ceccarelli, M. *et al.* Molecular Profiling Reveals Biologically Discrete Subsets and Pathways of Progression in Diffuse Glioma. *Cell* **164**, 550-563, doi:10.1016/j.cell.2015.12.028 (2016).

5 TCGA_Network *et al.* Comprehensive, Integrative Genomic Analysis of Diffuse Lower-Grade Gliomas. *The New England journal of medicine* **372**, 2481-2498, doi:10.1056/NEJMoa1402121 (2015).

6 Verhaak, R. G. *et al.* Integrated genomic analysis identifies clinically relevant subtypes of glioblastoma characterized by abnormalities in PDGFRA, IDH1, EGFR, and NF1. *Cancer cell* **17**, 98-110, doi:10.1016/j.ccr.2009.12.020 (2010).

7 Yan, H. *et al.* IDH1 and IDH2 mutations in gliomas. *The New England journal of medicine* **360**, 765-773, doi:10.1056/NEJMoa0808710 (2009).

8 Louis, D. N. *et al.* International Society Of Neuropathology--Haarlem consensus guidelines for nervous system tumor classification and grading. *Brain Pathol* **24**, 429-435, doi:10.1111/bpa.12171 (2014).

9 Louis, D. N. *et al.* The 2016 World Health Organization Classification of Tumors of the Central Nervous System: a summary. *Acta Neuropathol* **131**, 803-820, doi:10.1007/s00401-016-1545-1 (2016).

10 Venteicher, A. S. *et al.* Decoupling genetics, lineages, and microenvironment in IDH-mutant gliomas by single-cell RNA-seq. *Science* **355**, doi:10.1126/science.aai8478 (2017).

11 Patel, A. P. *et al.* Single-cell RNA-seq highlights intratumoral heterogeneity in primary glioblastoma. *Science* **344**, 1396-1401, doi:10.1126/science.1254257 (2014).

12 Snuderl, M. *et al.* Mosaic amplification of multiple receptor tyrosine kinase genes in glioblastoma. *Cancer cell* **20**, 810-817, doi:10.1016/j.ccr.2011.11.005 (2011).

13 Sottoriva, A. *et al.* Intratumor heterogeneity in human glioblastoma reflects cancer evolutionary dynamics. *Proceedings of the National Academy of Sciences of the United States of America* **110**, 4009-4014, doi:10.1073/pnas.1219747110 (2013).

14 Barthel, F. P., Wesseling, P. & Verhaak, R. G. W. Reconstructing the molecular life history of gliomas. *Acta Neuropathol* **135**, 649-670, doi:10.1007/s00401-018-1842-y (2018).

15 Williams, M. J. *et al.* Quantification of subclonal selection in cancer from bulk sequencing data. *Nat Genet* **50**, 895-903, doi:10.1038/s41588-018-0128-6 (2018).

16 Nejo, T. *et al.* Reduced Neoantigen Expression Revealed by Longitudinal Multiomics as a Possible Immune Evasion Mechanism in Glioma. *Cancer Immunol Res*, doi:10.1158/2326-6066.CIR-18-0599 (2019).
17 Alexandrov, L. B. *et al.* Signatures of mutational processes in human cancer. *Nature* **500**, 415-421, doi:10.1038/nature12477 (2013).
18 Wang, J. *et al.* Clonal evolution of glioblastoma under therapy. *Nat Genet* **48**, 768-776, doi:10.1038/ng.3590 (2016).
19 Kim, H. *et al.* Whole-genome and multisector exome sequencing of primary and post-treatment glioblastoma reveals patterns of tumor evolution. *Genome research* **25**, 316-327, doi:10.1101/gr.180612.114 (2015).
20 Johnson, B. E. *et al.* Mutational analysis reveals the origin and therapy-driven evolution of recurrent glioma. *Science* **343**, 189-193, doi:10.1126/science.1239947 (2014).
21 Hunter, C. *et al.* A hypermutation phenotype and somatic MSH6 mutations in recurrent human malignant gliomas after alkylator chemotherapy. *Cancer Res* **66**, 3987-3991, doi:10.1158/0008-5472.CAN-06-0127 (2006).
22 Jolly, C. & Van Loo, P. Timing somatic events in the evolution of cancer. *Genome Biol* **19**, 95, doi:10.1186/s13059-018-1476-3 (2018).
23 Turajlic, S., Sottoriva, A., Graham, T. & Swanton, C. Resolving genetic heterogeneity in cancer. *Nat Rev Genet*, doi:10.1038/s41576-019-0114-6 (2019).
24 Choi, S. *et al.* Temozolomide-associated hypermutation in gliomas. *Neuro Oncol* **20**, 1300-1309, doi:10.1093/neuonc/noy016 (2018).
25 Baumert, B. G. *et al.* Temozolomide chemotherapy versus radiotherapy in high-risk low-grade glioma (EORTC 22033-26033): a randomised, open-label, phase 3 intergroup study. *Lancet Oncol* **17**, 1521-1532, doi:10.1016/S1470-2045(16)30313-8 (2016).
26 Buckner, J. C. *et al.* Radiation plus Procarbazine, CCNU, and Vincristine in Low-Grade Glioma. *The New England journal of medicine* **374**, 1344-1355, doi:10.1056/NEJMoa1500925 (2016).
27 Ha, G. *et al.* TITAN: inference of copy number architectures in clonal cell populations from tumor whole-genome sequence data. *Genome research* **24**, 1881-1893, doi:10.1101/gr.180281.114 (2014).
28 Roth, A. *et al.* PyClone: statistical inference of clonal population structure in cancer. *Nat Methods* **11**, 396-398, doi:10.1038/nmeth.2883 (2014).
29 Martincorena, I. *et al.* Tumor evolution. High burden and pervasive positive selection of somatic mutations in normal human skin. *Science* **348**, 880-886, doi:10.1126/science.aaa6806 (2015).
30 Williams, M. J., Werner, B., Barnes, C. P., Graham, T. A. & Sottoriva, A. Identification of neutral tumor evolution across cancer types. *Nat Genet* **48**, 238-244, doi:10.1038/ng.3489 (2016).
31 Mermel, C. H. *et al.* GISTIC2.0 facilitates sensitive and confident localization of the targets of focal somatic copy-number alteration in human cancers. *Genome Biol* **12**, R41, doi:10.1186/gb-2011-12-4-r41 (2011).
32 Barthel, F. P. *et al.* Systematic analysis of telomere length and somatic alterations in 31 cancer types. *Nat Genet* **49**, 349-357, doi:10.1038/ng.3781 (2017).
33 Johannessen, T. A. *et al.* Rapid Conversion of Mutant IDH1 from Driver to Passenger in a Model of Human Gliomagenesis. *Molecular cancer research : MCR* **14**, 976-983, doi:10.1158/1541-7786.MCR-16-0141 (2016).
34 Luchman, H. A., Chesnelong, C., Cairncross, J. G. & Weiss, S. Spontaneous loss of heterozygosity leading to homozygous R132H in a patient-derived IDH1 mutant cell line. *Neuro Oncol* **15**, 979-980, doi:10.1093/neuonc/not064 (2013).

35 Mazor, T. *et al.* Clonal expansion and epigenetic reprogramming following deletion or amplification of mutant IDH1. *Proceedings of the National Academy of Sciences of the United States of America* **114**, 10743-10748, doi:10.1073/pnas.1708914114 (2017).

36 Korber, V. *et al.* Evolutionary Trajectories of IDH(WT) Glioblastomas Reveal a Common Path of Early Tumorigenesis Instigated Years ahead of Initial Diagnosis. *Cancer cell* **35**, 692-704 e612, doi:10.1016/j.ccell.2019.02.007 (2019).

37 deCarvalho, A. C. *et al.* Discordant inheritance of chromosomal and extrachromosomal DNA elements contributes to dynamic disease evolution in glioblastoma. *Nat Genet* **50**, 708-717, doi:10.1038/s41588-018-0105-0 (2018).

38 Giam, M. & Rancati, G. Aneuploidy and chromosomal instability in cancer: a jackpot to chaos. *Cell Div* **10**, 3, doi:10.1186/s13008-015-0009-7 (2015).

39 Taylor, A. M. *et al.* Genomic and Functional Approaches to Understanding Cancer Aneuploidy. *Cancer cell* **33**, 676-689 e673, doi:10.1016/j.ccell.2018.03.007 (2018).

40 Marty, R., Thompson, W. K., Salem, R. M., Zanetti, M. & Carter, H. Evolutionary Pressure against MHC Class II Binding Cancer Mutations. *Cell* **175**, 416-428 e413, doi:10.1016/j.cell.2018.08.048 (2018).

41 McGranahan, N. *et al.* Allele-Specific HLA Loss and Immune Escape in Lung Cancer Evolution. *Cell* **171**, 1259-1271 e1211, doi:10.1016/j.cell.2017.10.001 (2017).

42 Wang, Q. *et al.* Tumor Evolution of Glioma-Intrinsic Gene Expression Subtypes Associates with Immunological Changes in the Microenvironment. *Cancer cell* **32**, 42-56 e46, doi:10.1016/j.ccell.2017.06.003 (2017).

43 Rooney, M. S., Shukla, S. A., Wu, C. J., Getz, G. & Hacohen, N. Molecular and genetic properties of tumors associated with local immune cytolytic activity. *Cell* **160**, 48-61, doi:10.1016/j.cell.2014.12.033 (2015).

44 Dunn, G. P., Bruce, A. T., Ikeda, H., Old, L. J. & Schreiber, R. D. Cancer immunoediting: from immunosurveillance to tumor escape. *Nat Immunol* **3**, 991-998, doi:10.1038/ni1102-991 (2002).

45 Hundal, J. *et al.* pVAC-Seq: A genome-guided in silico approach to identifying tumor neoantigens. *Genome Med* **8**, 11, doi:10.1186/s13073-016-0264-5 (2016).

46 Rosenthal, R. *et al.* Neoantigen-directed immune escape in lung cancer evolution. *Nature* **567**, 479-485, doi:10.1038/s41586-019-1032-7 (2019).

47 Newman, A. M. *et al.* Robust enumeration of cell subsets from tissue expression profiles. *Nat Methods* **12**, 453-457, doi:10.1038/nmeth.3337 (2015).

48 Mazor, T. *et al.* DNA Methylation and Somatic Mutations Converge on the Cell Cycle and Define Similar Evolutionary Histories in Brain Tumors. *Cancer cell* **28**, 307-317, doi:10.1016/j.ccell.2015.07.012 (2015).

49 van den Bent, M. *et al.* Efficacy of depatuxizumab mafodotin (ABT-414) monotherapy in patients with EGFR-amplified, recurrent glioblastoma: results from a multi-center, international study. *Cancer Chemother Pharmacol* **80**, 1209-1217, doi:10.1007/s00280-017-3451-1 (2017).

50 Raub, T. J. *et al.* Brain Exposure of Two Selective Dual CDK4 and CDK6 Inhibitors and the Antitumor Activity of CDK4 and CDK6 Inhibition in Combination with Temozolomide in an Intracranial Glioblastoma Xenograft. *Drug Metab Dispos* **43**, 1360-1371, doi:10.1124/dmd.114.062745 (2015).

51 Miller, A. M. *et al.* Tracking tumour evolution in glioma through liquid biopsies of cerebrospinal fluid. *Nature* **565**, 654-658, doi:10.1038/s41586-019-0882-3 (2019).

52 Keskin, D. B. *et al.* Neoantigen vaccine generates intratumoral T cell responses in phase Ib glioblastoma trial. *Nature* **565**, 234-239, doi:10.1038/s41586-018-0792-9 (2019).

53 Schumacher, T. *et al.* A vaccine targeting mutant IDH1 induces antitumour immunity. *Nature* **512**, 324-327, doi:10.1038/nature13387 (2014).

54 Koster, J. & Rahmann, S. Snakemake-a scalable bioinformatics workflow engine. *Bioinformatics* **34**, 3600, doi:10.1093/bioinformatics/bty350 (2018).
55 Van der Auwera, G. A. *et al.* From FastQ data to high confidence variant calls: the Genome Analysis Toolkit best practices pipeline. *Curr Protoc Bioinformatics* **43**, 11 10 11-33, doi:10.1002/0471250953.bi1110s43 (2013).
56 Ewels, P., Magnusson, M., Lundin, S. & Kaller, M. MultiQC: summarize analysis results for multiple tools and samples in a single report. *Bioinformatics* **32**, 3047-3048, doi:10.1093/bioinformatics/btw354 (2016).
57 Li, H. *et al.* The Sequence Alignment/Map format and SAMtools. *Bioinformatics* **25**, 2078-2079, doi:10.1093/bioinformatics/btp352 (2009).
58 Beroukhim, R. *et al.* Assessing the significance of chromosomal aberrations in cancer: methodology and application to glioma. *Proceedings of the National Academy of Sciences of the United States of America* **104**, 20007-20012, doi:10.1073/pnas.0710052104 (2007).
59 Martincorena, I. *et al.* Universal Patterns of Selection in Cancer and Somatic Tissues. *Cell* **171**, 1029-1041 e1021, doi:10.1016/j.cell.2017.09.042 (2017).
60 Turajlic, S. *et al.* Tracking Cancer Evolution Reveals Constrained Routes to Metastases: TRACERx Renal. *Cell* **173**, 581-594 e512, doi:10.1016/j.cell.2018.03.057 (2018).
61 Szolek, A. *et al.* OptiType: precision HLA typing from next-generation sequencing data. *Bioinformatics* **30**, 3310-3316, doi:10.1093/bioinformatics/btu548 (2014).
62 Hoof, I. *et al.* NetMHCpan, a method for MHC class I binding prediction beyond humans. *Immunogenetics* **61**, 1-13, doi:10.1007/s00251-008-0341-z (2009).

Figure Legends

Fig. 1 | **Temporal changes in glioma mutational rates and processes. a**. Each column represents a single patient (*n* = 222) at two separate timepoints grouped by glioma subtype and ordered left-to-right by decreasing mutation frequency at recurrence. Top, mutation frequency differences between initial and recurrent tumors. Blue dotted line indicates increased mutation frequency while a red dotted line indicates decreased mutational frequency. Stacked bar plot reflects the proportion of total mutations shared (mustard), private to initial (magenta), or private to recurrence (blue). Clinical information including hypermutation status, therapy, and grade changes. **b**. Stacked bar plot (n=219) indicating the dominant mutational signature among initial, recurrent and shared mutation fractions stratified by glioma subtype. **c**. The proportion of glioma recurrences with alkylating agent-related hypermutation, grouped by glioma subtype. Fisher's exact test was used to compare proportions between subtypes. **d**. Kaplan-Meier curve depicting overall survival in hypermutant (red) versus non-hypermutant (blue) patients amongst IDHwt (left, *n* = 99) and IDHmut-noncodel (right, *n* = 32) tumors. Log-rank test P-values are shown.

Fig. 2 | **Quantifying selective pressures during glioma evolution. a**. Schematic depiction of cancer cell fraction (CCF) values during tumor evolution indicating clonality and associated relative timing. **b.** Comparison of PyClone clusters ranked by CCF in matched initial and recurrent tumors. **c**. *Left*: dN/dS ratio for all variants (i.e. global) in initial and recurrent tumors for each subtype. Hypermutators were not included (*n* = 187). Dots represent the global dN/dS ratio with associated Wald confidence intervals. *Right*: global dN/dS ratios for variant fractions per subtype. **d.** Cumulative distribution of subclonal mutations by their inverse variant allele

frequency. Mutations were separated by timepoint, variant fraction, and glioma subtype. Deviation from a linear relationship, significant Kolmogorov-Smirnov P-values and R^2 below 0.98 indicate selection. **e.** Sankey plot indicating the breakdown of SubClonalSelection evolutionary modes by subtype and therapy (*n* = 104). The sizes of the bands reflect sample sizes and band colors highlight the glioma subtype. Gray coloring reflects instances when treatment information was not available. **f.** Kaplan-Meier curve showing survival differences between IDHwt recurrent tumors demonstrating selection (*n* = 39) compared with neutrally evolving tumors (*n* = 44). Log-rank P-value is indicated.

Fig. 3 | **Patterns of glioma driver frequencies over time. a.** Driver dynamics for SNVs nominated by the dNdScv and CNVs nominated by GISTIC (*n* = 222). Each column represents a single patient at two separate time points stratified by subtype and ordered left-to-right by the number of driver alterations. The degree of aneuploidy difference (recurrence – initial) offers a summary metric for increases (> 0) or decreases (< 0) in aneuploidy at recurrence. Variants are marked and different shapes indicate whether a variant was shared or private. The variant type is depicted by its color. Stacked bar plots accompanying each gene/arm provide cohort-level proportions for whether the alteration was shared, lost, or acquired. **b.** Aneuploidy comparison in matching initial and recurrent IDHmut-noncodel tumors. **c.** Within-sample CCF comparison of *CDKN2A* homozygous deletion (homdel) to genome-wide CCF as a proxy for aneuploidy. A relative higher CCF indicates temporal precedence. Wilcoxon signed-rank test P-value is indicated. **d.** Kaplan-Meier curve comparing survival in IDHmut-noncodel tumors with an alteration in the cell cycle, acquired aneuploidy, or both (shades of red) versus unaltered IDHmut-noncodel tumors (blue). Log-rank P-value is shown.

Fig. 4 | **Neoantigen selection is stable throughout tumor progression. a.** Mean proportion of coding mutations giving rise to neoantigens (neoantigens/nonsynonymous) stratified by glioma subtype and timepoint (*n* = 222). Error bars represent standard deviation. **b.** Boxplot depicting the distribution of observed to expected neoantigen ratios in the GLASS cohort stratified by glioma subtype. P-value was calculated using the Wilcoxon rank-sum test. Each box spans quartiles, with the lines representing the median ratio for each group. Whiskers represent absolute range, excluding outliers. **c.** Scatterplot depicting the association between the observed to expected neoantigen ratio in a patient's initial versus recurrent tumor. Each point represents a single patient. R represents Pearson correlation coefficient. Panels b and c only include samples with at least 3 neoantigens in the initial and recurrent tumors (*n* = 131, 63, and 24 for IDHwt, IDHmut-noncodel, and IDHmut-codel, respectively). **d.** Ladder plot depicting the difference in observed to expected neoantigen ratio between a tumor's clonal and subclonal neoantigens. Each set of points connected by a line represents one tumor. Tumors are stratified by whether they were a patient's initial or recurrent tumor. Lines are colored by each patient's glioma subtype. Panel d only includes samples with at least 3 clonal neoantigens and at least 3 subclonal neoantigens in both the initial and recurrent tumors (*n* = 35, 20 and 9 for IDHwt, IDHmut-noncodel, and IDHmut-codel, respectively). Colors in each panel represent the glioma subtype and are denoted in panel d.

Extended Data Fig. 1 | **Sample Selection. a.** Quality control workflow steps identifying all GLASS samples available as a resource and the identification of the highest quality set of

patient pairs (*n* = 222) used for the presented mutational and copy number analyses. **b.** Additional available datasets.

Extended Data Fig. 2 | **Mutation rate by time point and subtype. a.** Boxplots and paired lines depicting coverage adjusted mutation frequencies in initial and matched recurrent samples across three subtypes. Wilcoxon signed-rank test P-values and sample sizes are indicated. **b.** Bee swarm plot depicting coverage adjusted mutation frequencies in fractions by subtype. Dashed line indicates the mean. One-way ANOVA P-values comparing three subtypes are indicated. **c.** Scatter plot showing the relationship between age at diagnosis and coverage adjusted mutation rates by subtype and fraction. Linear model P-values are indicated and were adjusted by subtype. **d.** Similar to the analysis presented in **c**, but showing the relationship between time to recurrence and coverage adjusted mutation rates.

Extended Data Fig. 3 | **Mutational signatures by fraction and subtype. a.** Correlation plot showing the Pearson's chi-squared (X^2) residuals for each signature by fraction and subtype. A X^2 was performed for each subtype and P-values are indicated. Positive residuals (blue) indicate a positive correlation, whereas negative residuals (red) indicate an anticorrelation. The point size reflects the contribution to X^2 estimate. **b.** The same ordered of patients as Fig. 1a along with relevant clinical information is provided alongside the fraction-specific mutational signatures. PyClone mutational clusters are also presented.

Extended Data Fig. 4 | **Hypermutator clonality. a.** Bar plots represent counts of recurrence-only mutations per hypermutator tumor that were known to receive alkylating agent therapy and were successfully run through the PyClone algorithm. Colors indicate mutation clonality and color intensity indicates whether the mutations resulted in coding changes. **b.** Kaplan-Meier curve comparing alkylating agent-treated patients with IDHmut-noncodel hypermutator tumors that were predominantly clonal (*n* = 8), predominantly subclonal (*n* = 7), versus IDHmut-noncodel non-hypermutators known to be treated with alkylating agents and had available PyClone data (*n* = 17). Log-rank P-value is shown.

Extended Data Fig. 5 | **Clonal structure evolution over time**. **a.** The minimum cancer cell fraction of the most persistent (shared between initial and recurrence) PyClone cluster. **b.** Comparison of PyClone clusters ranked by CCF in matched initial and recurrent tumors, as Fig. 2b but separated by subtype. **c-d.** Examples of cluster CCF dynamics over time in three separate samples, including **(c)** two multi-timepoint samples **(d)** and one multi-sector sample. These additional data are available in the GLASS resource, but only two time-separated samples were used throughput the manuscript to ensure clarity.

Extended Data Fig. 6 | **Variant allele fraction distribution (a)** Non-hypermutator variant allele fraction distributions for copy neutral variants in coding regions (n = 181 patients). Variants are separated by subtype, fraction, and also whether the variant was non-synonymous or synonymous mutation in a coding region. R^2 goodness-of-fit measure and associated P-values are shown for both mutation types. Note that this data considers only the coding portion of genome while Fig. 2d presents both coding and non-coding. **(b)** The cumulative distribution of the subclonal mutations in copy-neutral regions for hypermutators (n = 31 patients). For each variant fraction and subtype, the R^2 goodness-of-fit measure and P-values are shown.

Extended Data Fig. 7 | **Driver gene nomination. a.** Local (gene-wise) dN/dScv estimates by subtype (rows) and fraction (columns). Genes are sorted by Q-value and P-value. The Q-value is shown in color, whereas the P-value is indicated in light gray. The Q-value threshold of 0.05 is indicated by a horizontal red line. **b.** GISTIC significant amplification (red) and deletion (blue) plots in initial (left) and recurrent tumors (right). Chromosomal locations are ordered on the y-axis, Q-values are shown on the x-axis, and selected drivers are indicated by their chromosomal location on the right.

Extended Data Fig. 8 | **Driver acquisition over time a.** Tabulated numbers of SNV (top) and CNV (bottom) driver events that were shared, initial-only, or recurrence-only. P-values were obtained using a two-sided Fisher test comparing the initial-only fraction to the recurrence-only fraction testing for acquisition. **b.** One-sided Fisher test comparing the initial-only fraction to the recurrence-only fraction amongst previously implicated glioma drivers testing for driver acquisition. P-values were adjusted for multiple testing using the FDR (x-axis). Hypermutators (red) and non-hypermutators (black) were separately analyzed.

Extended Data Fig. 9 | **Intra-tumor CCF comparison.** Ladder plots comparing the CCF of co-occurring drivers in single tumor samples. The color of the lines and points indicates whether the sample shown is an initial (brown) or recurrent (green) tumor. Two-sided Wilcoxon rank-sum test P-values are shown for all initial samples, all recurrent samples, as well as all samples (black).

Extended Data Fig. 10 | **Inter-tumor CCF comparison. a.** Driver-gene CCF comparison between initial and matched recurrences. Lines are colored by variant classification. Two-sided Wilcoxon rank-sum test P-values are shown. **b.** *TP53* CCF by subtype, otherwise as in **(a)**. **c.** *IDH1* CCF by subtype, otherwise as in **(a)**. **d.** Ladder plot visualizing CCF change across all SNVs between initial and recurrent tumors, separated by subtype. Wilcoxon rank-sum test was used to test for differences between time points. **e.** Initial and recurrent mutations in each patient were compared using a Wilcoxon rank-sum test. Bar plot with counts of patients in each subtype are shown. Patients lacking significant change are shown in yellow, those with a significant increase or decrease are shown in dark and light blue, respectively.

Extended Data Fig. 11 | **Aneuploidy calculation a.** Heatmap displaying the chromosomal arm-level events (x-axis) with patients represented in each row. Patients are placed in the same order for both the initial (left) and recurrence (right). White space was inserted as a break between the three subtypes. **b.** Distribution of total aneuploidy difference. Acquired aneuploidy determination (upper-quartile) indicated with a red line. **c.** Comparison of aneuploidy score between initial and recurrent tumors separated by subtype **d.** As **(c)**, comparing aneuploidy value.

Extended Data Fig. 12 | **Neoantigen evolution and cellular analysis a.** Bar plots present the number of shared mutations that give rise to neoantigens (top row, “immunogenic”) and those that do not give rise to neoantigens (bottom row, “non-immunogenic”) broken down by longitudinal clonality (“(clonality in initial)-(clonality in recurrence)”) and separated by subtype.

Percentage of longitudinal clonality per subtype and mutation immunogenicity are presented above the respective bars. **b.** *Left:* Ladder plot depicting the difference in observed to expected neoantigen ratio between the initial and recurrent tumors of patients with hypermutated tumors at recurrence. Each set of points connected by a line represents one tumor (n =70). *Right:* Boxplot depicting the distribution of observed to expected neoantigen ratios in recurrent tumors stratified by hypermutator status (n = 35 and 183 for hypermutators and non-hypermutators, respectively). Each box spans quartiles, with the lines representing the median ratio for each group. Whiskers represent absolute range, excluding outliers. P-values for panel b were calculated using the Wilcoxon rank-sum test. **c.** Stacked bar plots depicting the average relative fraction of 11 CIBERSORT cell types in the neoantigen depleted (< 1) and non-depleted (> 1) initial and recurrent tumor subgroups. Asterisks indicate a significant difference between the depleted and non-depleted groups for that cell type at that time.

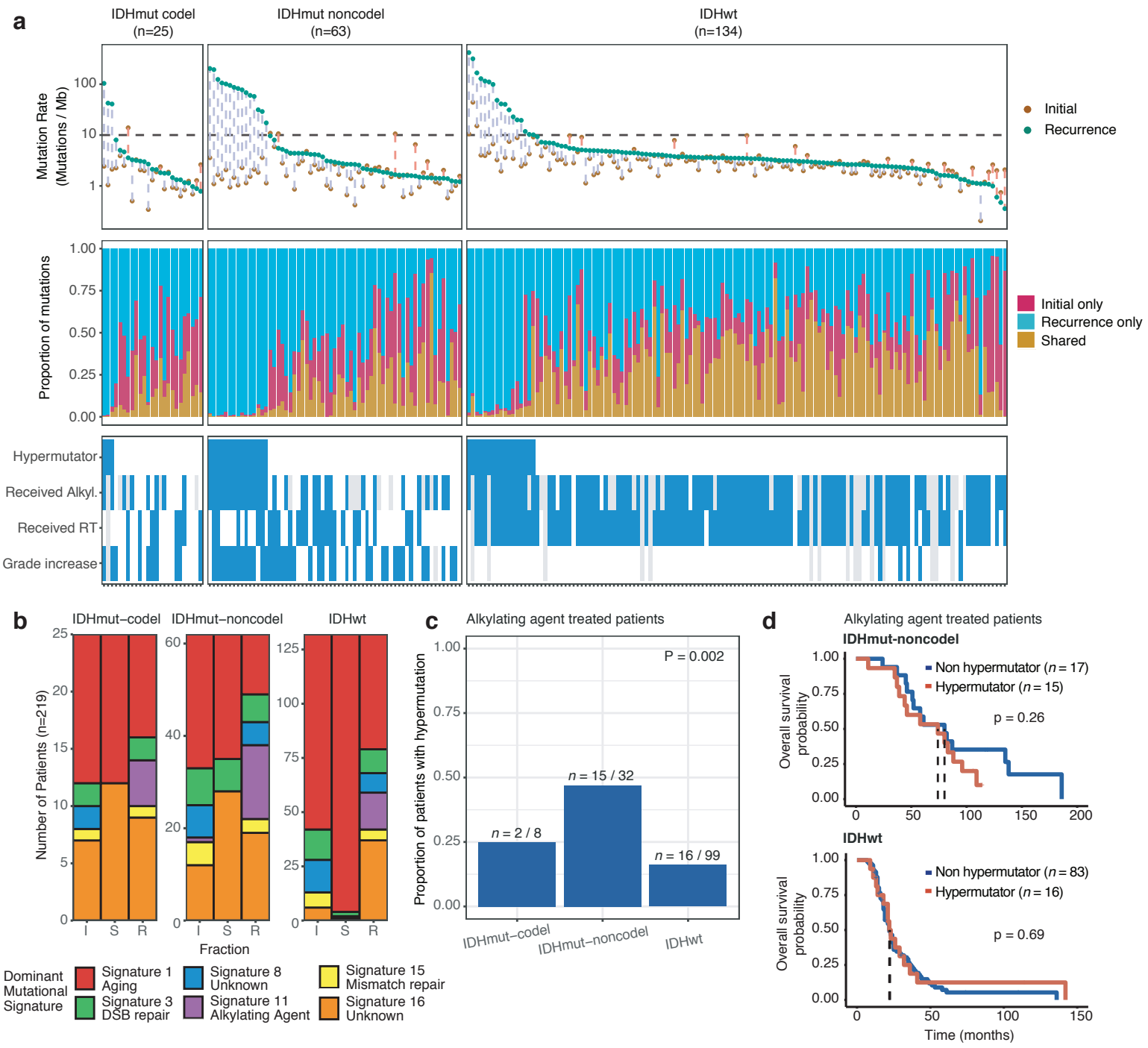

Fig. 1 | Temporal changes in glioma mutational rates and processes. a. Each column represents a single patient (n = 222) at two separate timepoints grouped by glioma subtype and ordered left-to-right by decreasing mutation frequency at recurrence. Top, mutation frequency differences between initial and recurrent tumors. Blue dotted line indicates increased mutation frequency while a red dotted line indicates decreased mutational frequency. Stacked bar plot reflects the proportion of total mutations shared (mustard), private to initial (magenta), or private to recurrence (blue). Clinical information including hypermutation status, therapy, and grade changes. b. Stacked bar plot (n=219) indicating the dominant mutational signature among initial, recurrent and shared mutation fractions stratified by glioma subtype. c. The proportion of glioma recurrences with alkylating agent-related hypermutation, grouped by glioma subtype. Fisher's exact test was used to compare proportions between subtypes. d. Kaplan-Meier curve depicting overall survival in hypermutant (red) versus non-hypermutant (blue) patients amongst IDHwt (left, n = 99) and IDHmut-noncodel (right, n = 32) tumors. Log-rank test P-values are shown.

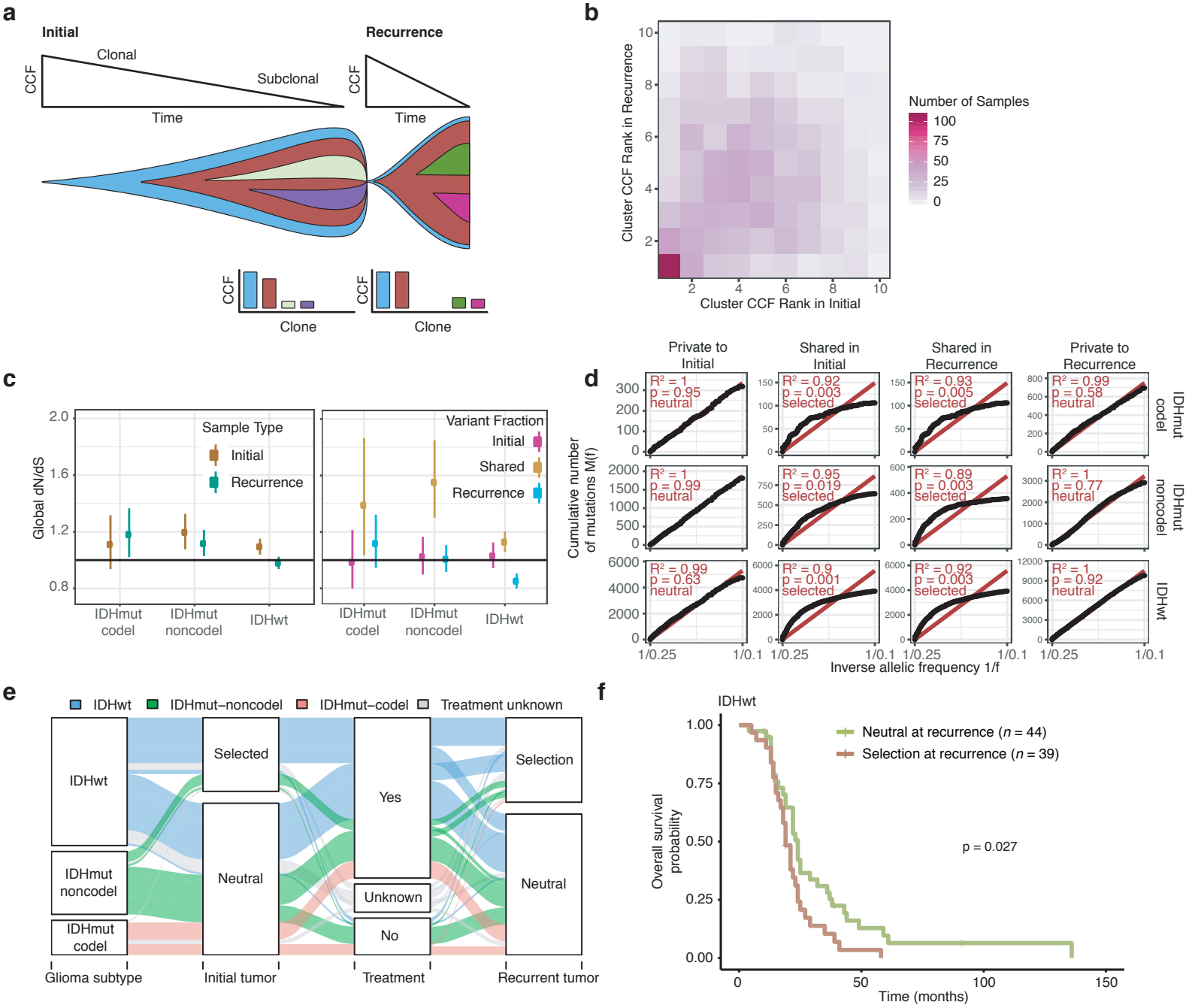

Fig. 2 | Quantifying selective pressures during glioma evolution. a. Schematic depiction of cancer cell fraction (CCF) values during tumor evolution indicating clonality and associated relative timing. b. Comparison of PyClone clusters ranked by CCF in matched initial and recurrent tumors. c. Left: dN/dS ratio for all variants (i.e. global) in initial and recurrent tumors for each subtype. Hypermutators were not included (n = 187). Dots represent the global dN/dS ratio with associated Wald confidence intervals. Right: global dN/dS ratios for variant fractions per subtype. d. Cumulative distribution of subclonal mutations by their inverse variant allele frequency. Mutations were separated by timepoint, variant fraction, and glioma subtype. Deviation from a linear relationship, significant Kolmogorov-Smirnov P-values and R2 below 0.98 indicate selection. e. Sankey plot indicating the breakdown of SubClonalSelection evolutionary modes by subtype and therapy (n = 104). The sizes of the bands reflect sample sizes and band colors highlight the glioma subtype. Gray coloring reflects instances when treatment information was not available. f. Kaplan-Meier curve showing survival differences between IDHwt recurrent tumors demonstrating selection (n = 39) compared with neutrally evolving tumors (n = 44). Log-rank P-value is indicated.

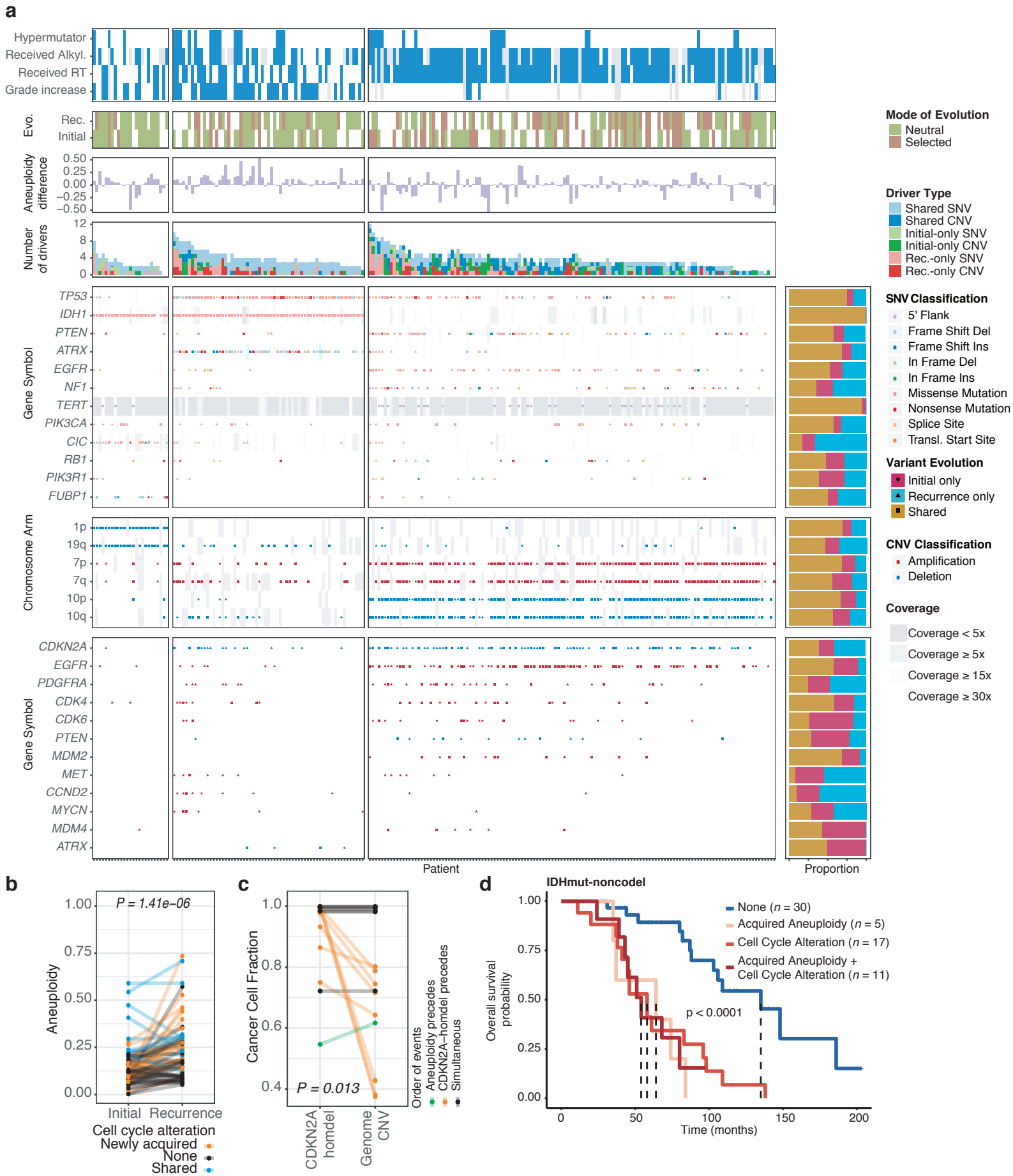

Fig. 3 | Patterns of glioma driver frequencies over time. a. Driver dynamics for SNVs nominated by the dNdScv and CNVs nominated by GISTIC (n = 222). Each column represents a single patient at two separate time points stratified by subtype and ordered left-to-right by the number of driver alterations. The degree of aneuploidy difference (recurrence – initial) offers a summary metric for increases (> 0) or decreases (< 0) in aneuploidy at recurrence. Variants are marked and different shapes indicate whether a variant was shared or private. The variant type is depicted by its color. Stacked bar plots accompanying each gene/arm provide cohort-level proportions for whether the alteration was shared, lost, or acquired. b. Aneuploidy comparison in matching initial and recurrent IDHmut-noncodel tumors. c. Within-sample CCF comparison of CDKN2A homozygous deletion (homdel) to genome-wide CCF as a proxy for aneuploidy. A relative higher CCF indicates temporal precedence. Wilcoxon signed-rank test P-value is indicated. d. Kaplan-Meier curve comparing survival in IDHmut-noncodel tumors with an alteration in the cell cycle, acquired aneuploidy, or both (shades of red) versus unaltered IDHmut-noncodel tumors (blue). Log-rank P-value is shown.

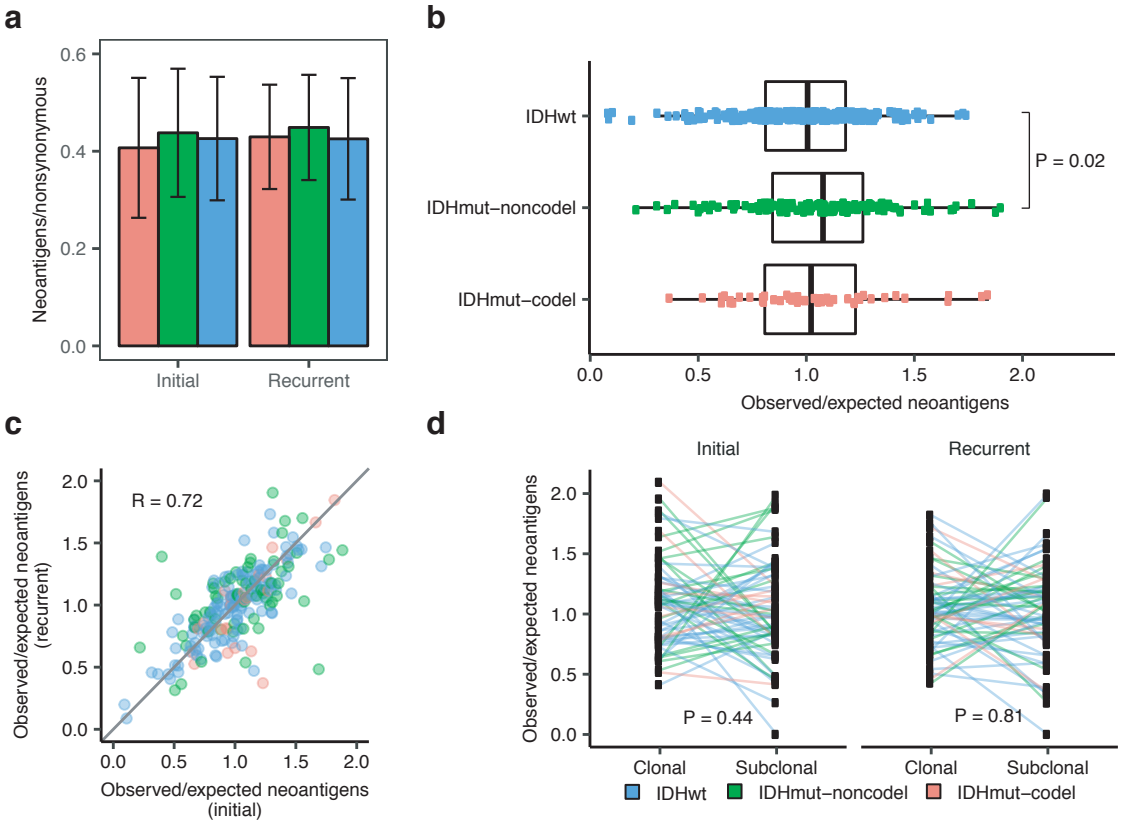

Fig. 4 | Neoantigen selection is stable throughout tumor progression. a. Mean proportion of coding mutations giving rise to neoantigens (neoantigens/nonsynonymous) stratified by glioma subtype and timepoint (n = 222). Error bars represent standard deviation. b. Boxplot depicting the distribution of observed to expected neoantigen ratios in the GLASS cohort stratified by glioma subtype. P-value was calculated using the Wilcoxon rank-sum test. Each box spans quartiles, with the lines representing the median ratio for each group. Whiskers represent absolute range, excluding outliers. c. Scatterplot depicting the association between the observed to expected neoantigen ratio in a patient's initial versus recurrent tumor. Each point represents a single patient. R represents Pearson correlation coefficient. Panels b and c only include samples with at least 3 neoantigens in the initial and recurrent tumors (n = 131, 63, and 24 for IDHwt, IDHmut-noncodel, and IDHmut-codel, respectively). d. Ladder plot depicting the difference in observed to expected neoantigen ratio between a tumor's clonal and subclonal neoantigens. Each set of points connected by a line represents one tumor. Tumors are stratified by whether they were a patient's initial or recurrent tumor. Lines are colored by each patient's glioma subtype. Panel d only includes samples with at least 3 clonal neoantigens and at least 3 subclonal neoantigens in both the initial and recurrent tumors (n = 35, 20 and 9 for IDHwt, IDHmut-noncodel, and IDHmut-codel, respectively). Colors in each panel represent the glioma subtype and are denoted in panel d.

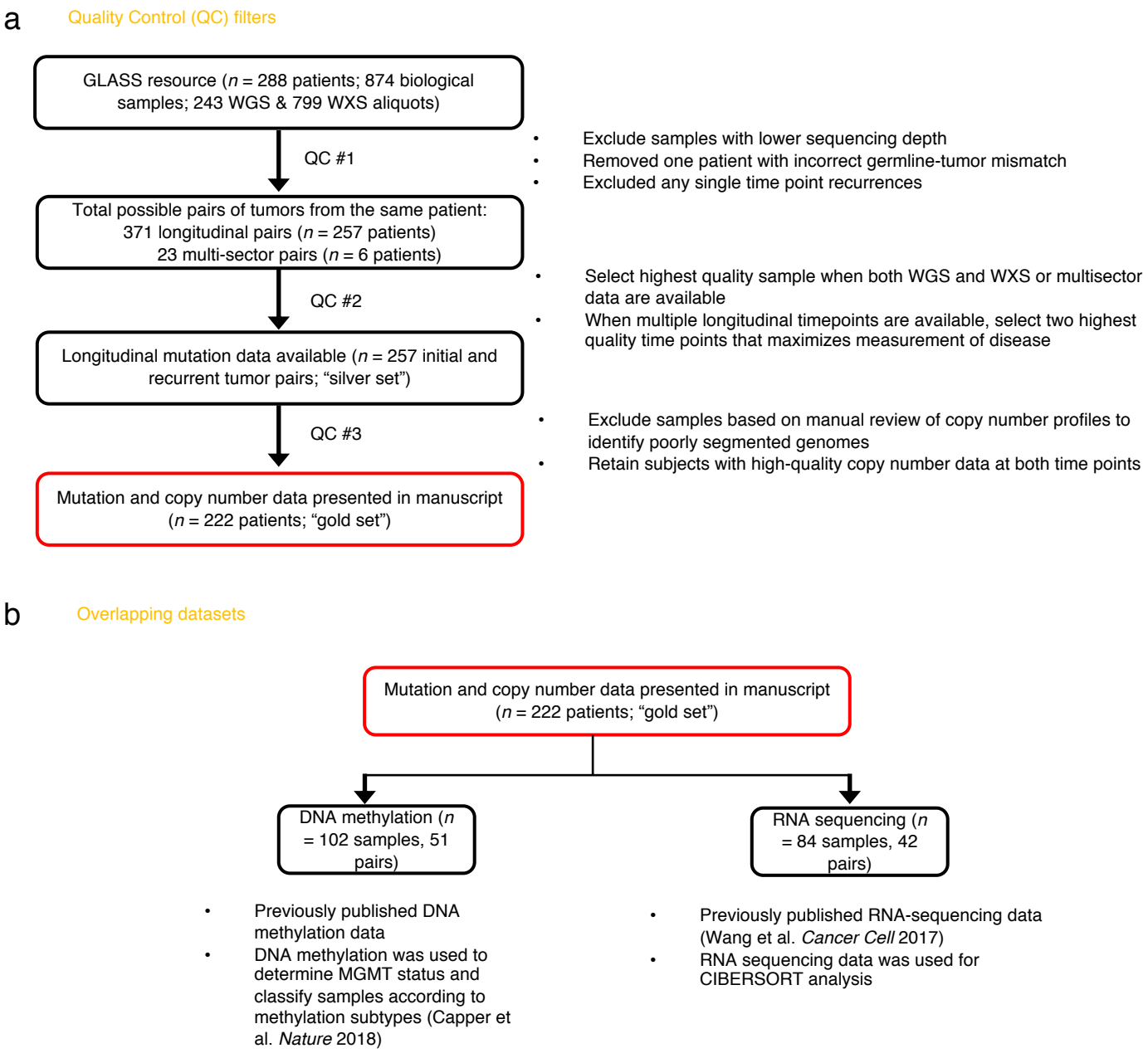

Extended Data Fig. 1 | Sample Selection. a. Quality control workflow steps identifying all GLASS samples available as a resource and the identification of the highest quality set of patient pairs (n = 222) used for the presented mutational and copy number analyses. b. Additional available datasets.

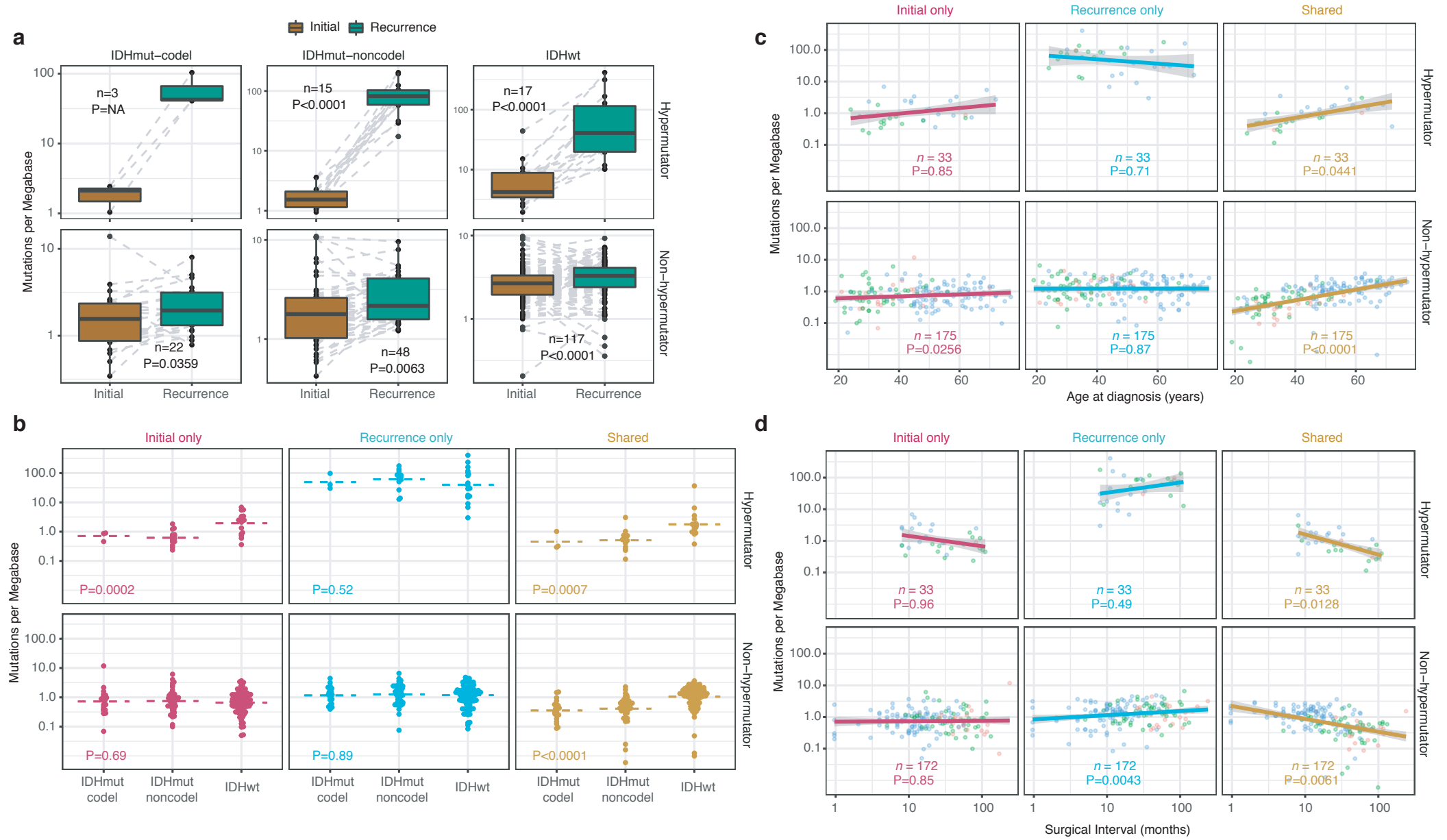

Extended Data Fig. 2 | Mutation rate by time point and subtype. a. Boxplots and paired lines depicting coverage adjusted mutation frequencies in initial and matched recurrent samples across three subtypes. Wilcoxon signed-rank test P-values and sample sizes are indicated. b. Bee swarm plot depicting coverage adjusted mutation frequencies in fractions by subtype. Dashed line indicates the mean. One-way ANOVA P-values comparing three subtypes are indicated. c. Scatter plot showing the relationship between age at diagnosis and coverage adjusted mutation rates by subtype and fraction. Linear model P-values are indicated and were adjusted by subtype. d. Similar to the analysis presented in c, but showing the relationship between time to recurrence and coverage adjusted mutation rates.

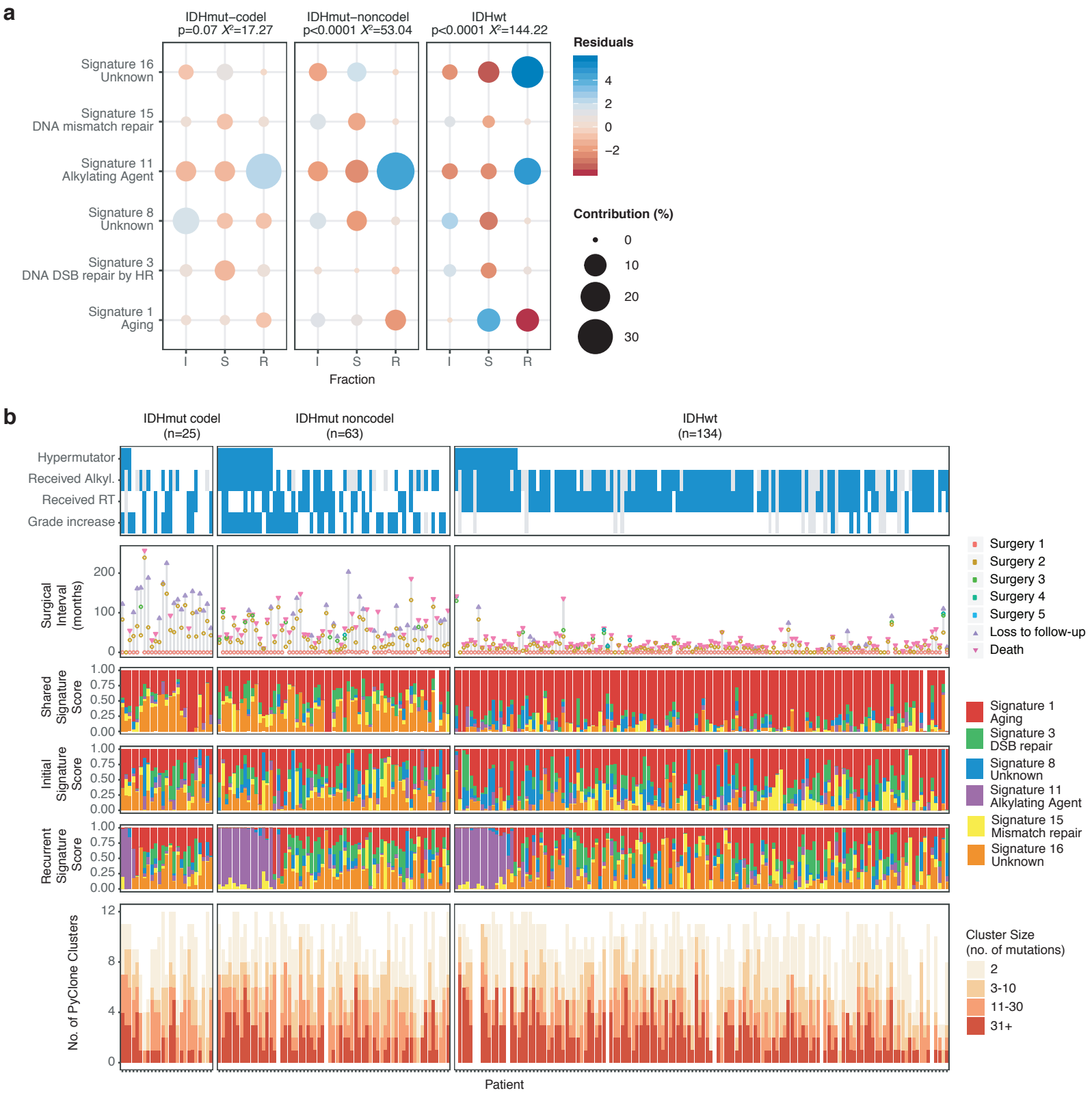

Extended Data Fig. 3 | Mutational signatures by fraction and subtype. a. Correlation plot showing the Pearson's chi-squared (X2) residuals for each signature by fraction and subtype. A X2 was performed for each subtype and P-values are indicated. Positive residuals (blue) indicate a positive correlation, whereas negative residuals (red) indicate an anticorrelation. The point size reflects the contribution to X2 estimate. b. The same ordered of patients as Fig. 1a along with relevant clinical information is provided alongside the fraction-specific mutational signatures. PyClone mutational clusters are also presented.

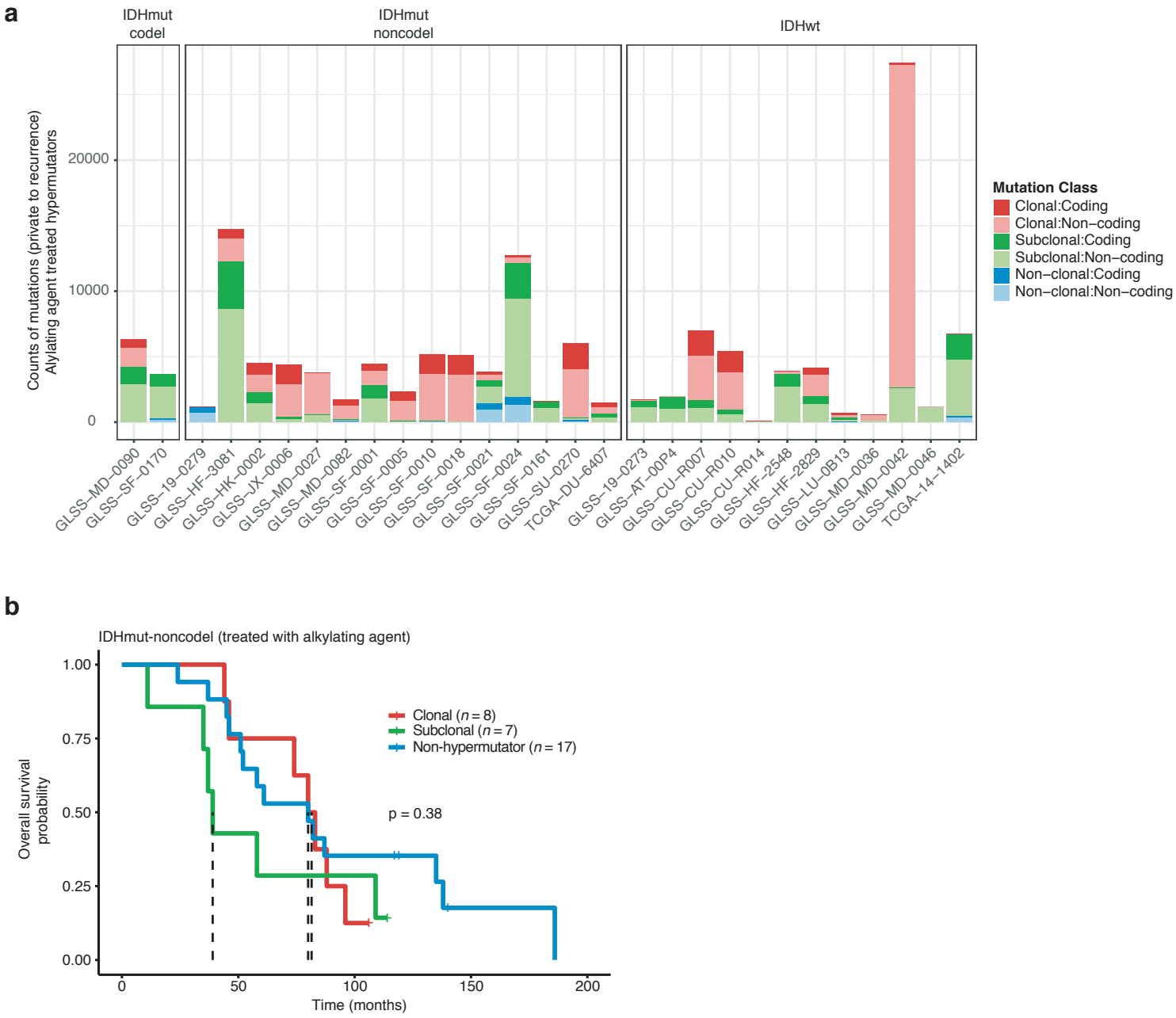

Extended Data Fig. 4 | Hypermutator clonality. a. Bar plots represent counts of recurrence-only mutations per hypermutator tumor that were known to receive alkylating agent therapy and were successfully run through the PyClone algorithm. Colors indicate mutation clonality and color intensity indicates whether the mutations resulted in coding changes. b. Kaplan-Meier curve comparing alkylating agent-treated patients with IDHmut-noncodel hypermutator tumors that were predominantly clonal (n = 8), predominantly subclonal (n = 7), versus IDHmut-noncodel non-hypermutators known to be treated with alkylating agents and had available PyClone data (n = 17). Log-rank P-value is shown.

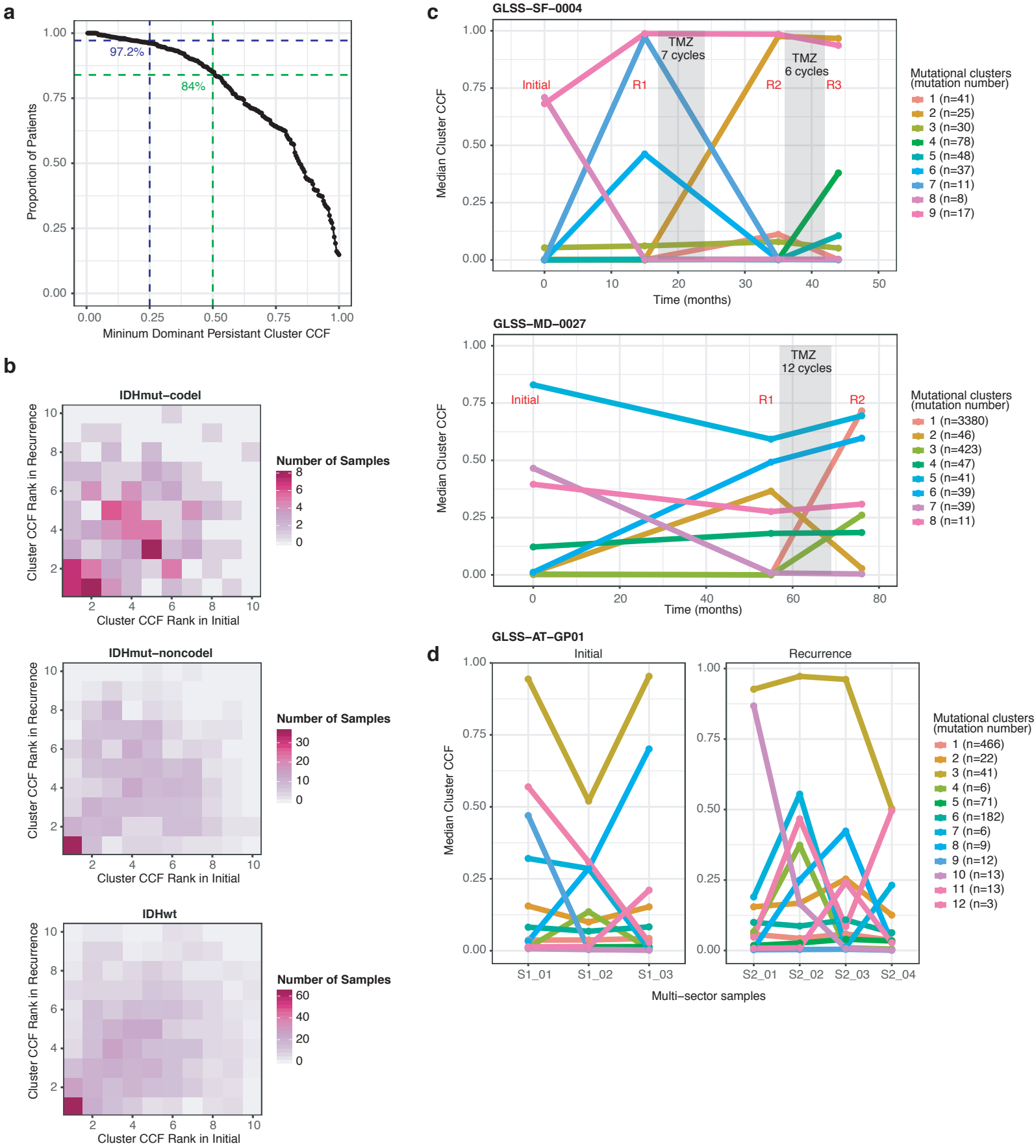

Extended Data Fig. 5 | Clonal structure evolution over time. a. The minimum cancer cell fraction of the most persistent (shared between initial and recurrence) PyClone cluster. b. Comparison of PyClone clusters ranked by CCF in matched initial and recurrent tumors, as Fig. 2b but separated by subtype. c-d. Examples of cluster CCF dynamics over time in three separate samples, including (c) two multi-timepoint samples (d) and one multi-sector sample. These additional data are available in the GLASS resource, but only two time-separated samples were used throughput the manuscript to ensure clarity.

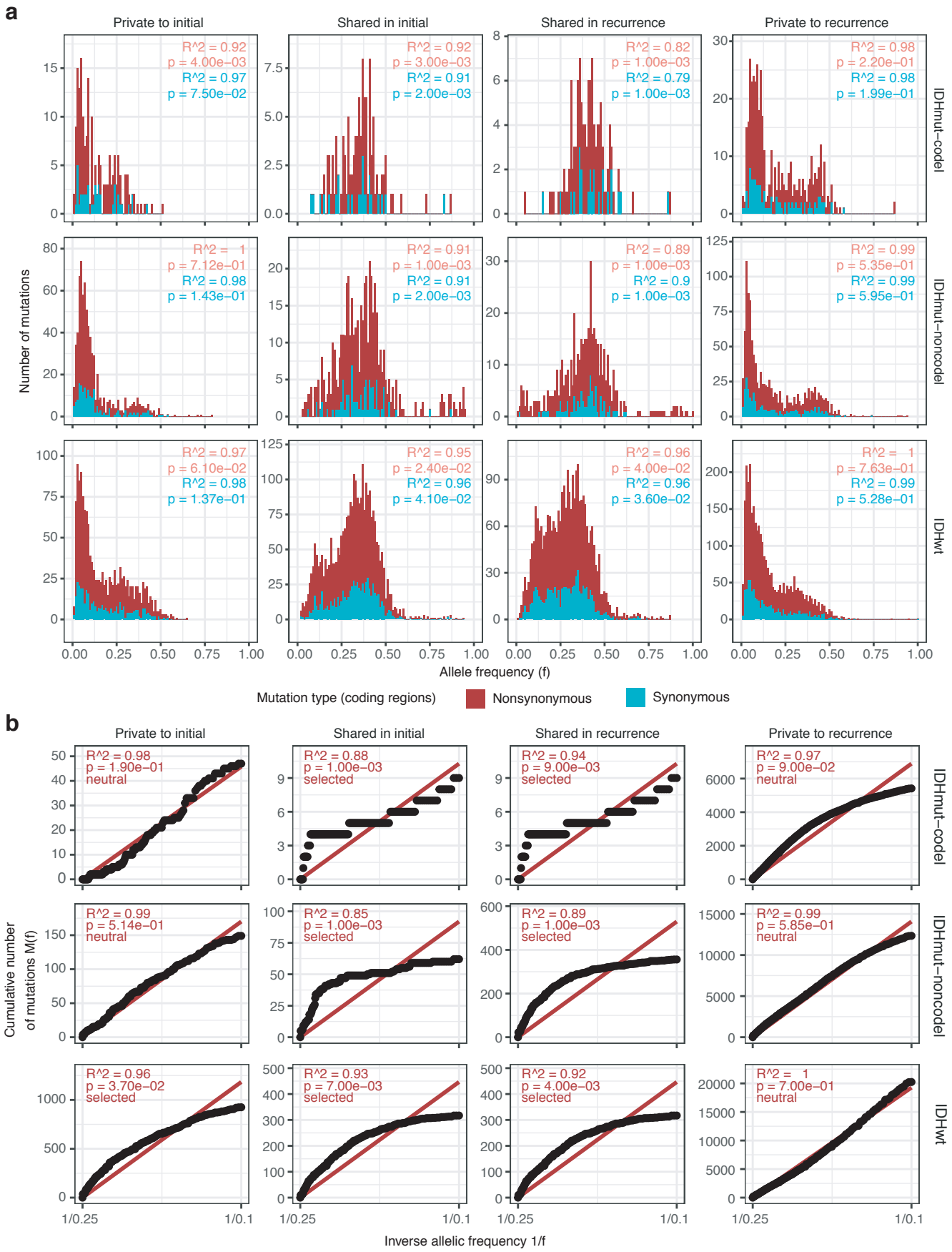

Extended Data Fig. 6 | Variant allele fraction distribution (a) Non-hypermutator variant allele fraction distributions for copy neutral variants in coding regions (n = 181 patients). Variants are separated by subtype, fraction, and also whether the variant was non-synonymous or synonymous mutation in a coding region. R2 goodness-of-fit measure and associated P-values are shown for both mutation types. Note that this data considers only the coding portion of genome while Fig. 2d presents both coding and non-coding. (b) The cumulative distribution of the subclonal mutations in copy-neutral regions for hypermutators (n = 31 patients). For each variant fraction and subtype, the R2 goodness-of-fit measure and P-values are shown.

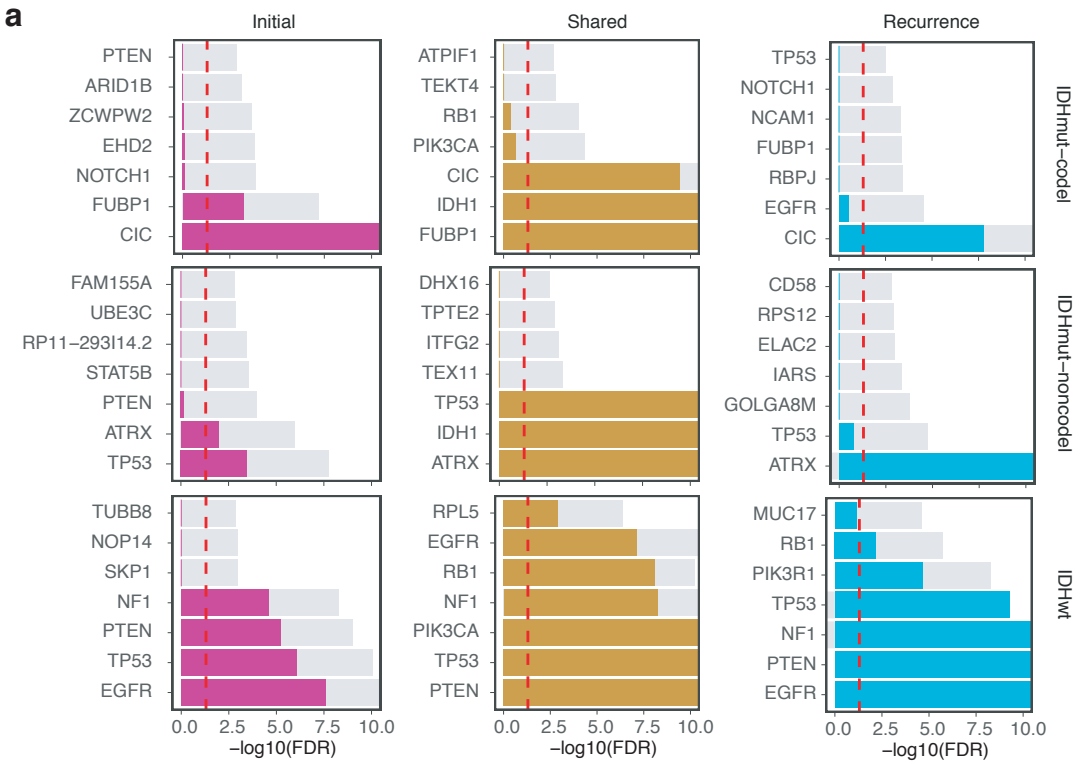

Extended Data Fig. 7 | Driver gene nomination. a. Local (gene-wise) dN/dScv estimates by subtype (rows) and fraction (columns). Genes are sorted by Q-value and P-value. The Q-value is shown in color, whereas the P-value is indicated in light gray. The Q-value threshold of 0.05 is indicated by a horizontal red line. b. GISTIC significant amplification (red) and deletion (blue) plots in initial (left) and recurrent tumors (right). Chromosomal locations are ordered on the y-axis, Q-values are shown on the x-axis, and selected drivers are indicated by their chromosomal location on the right.

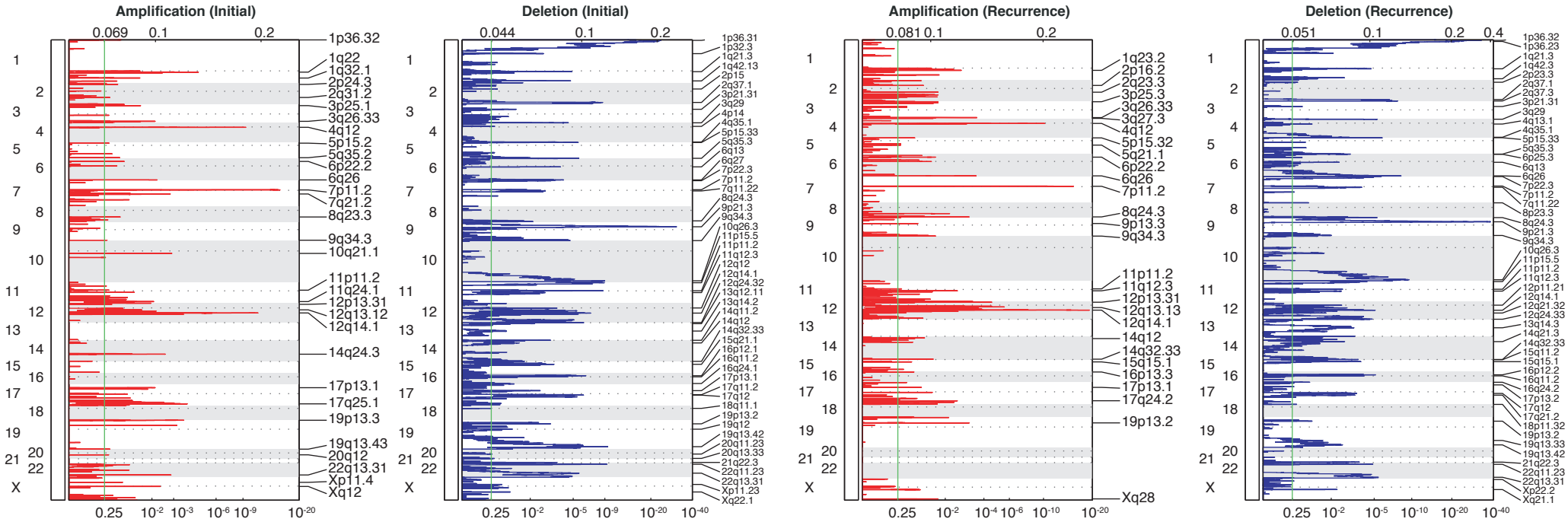

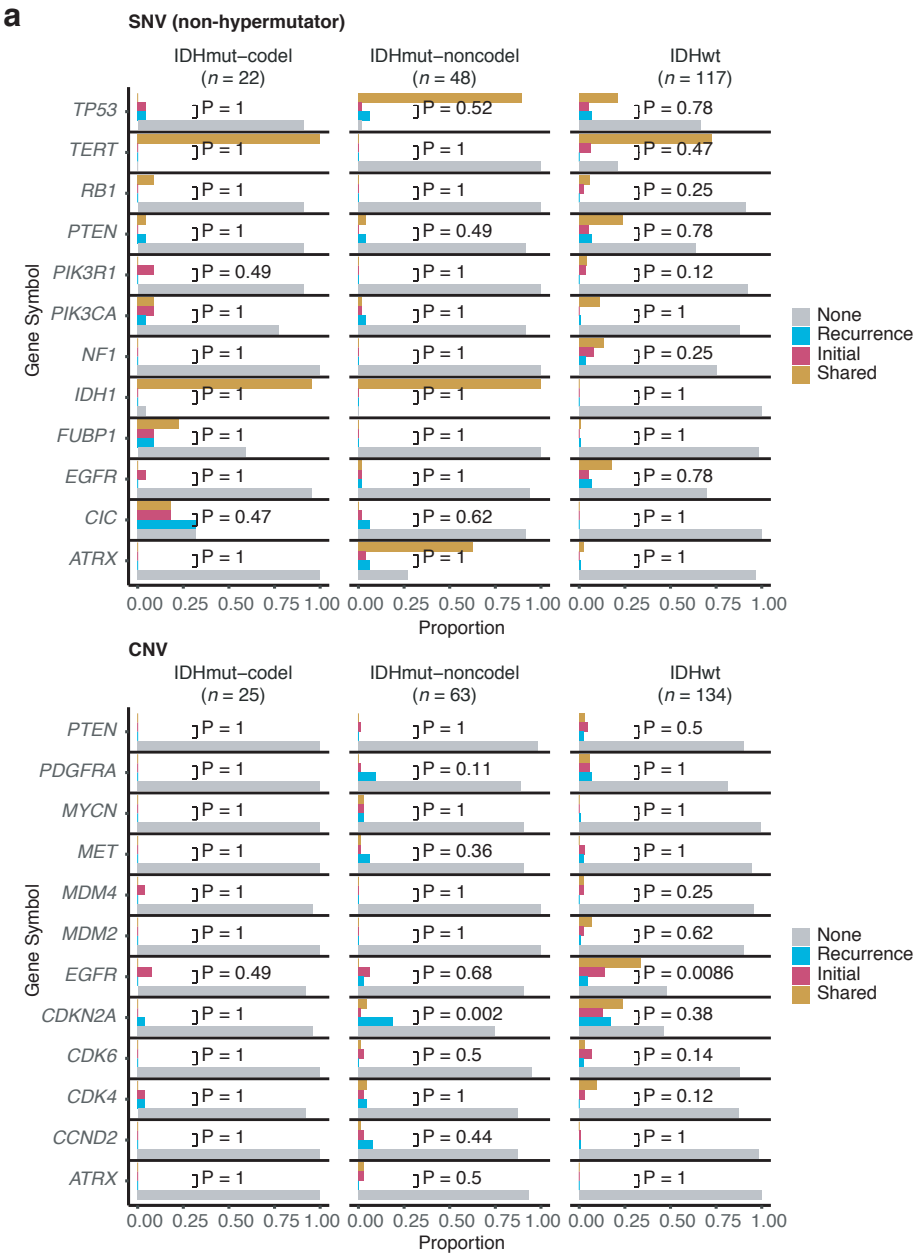

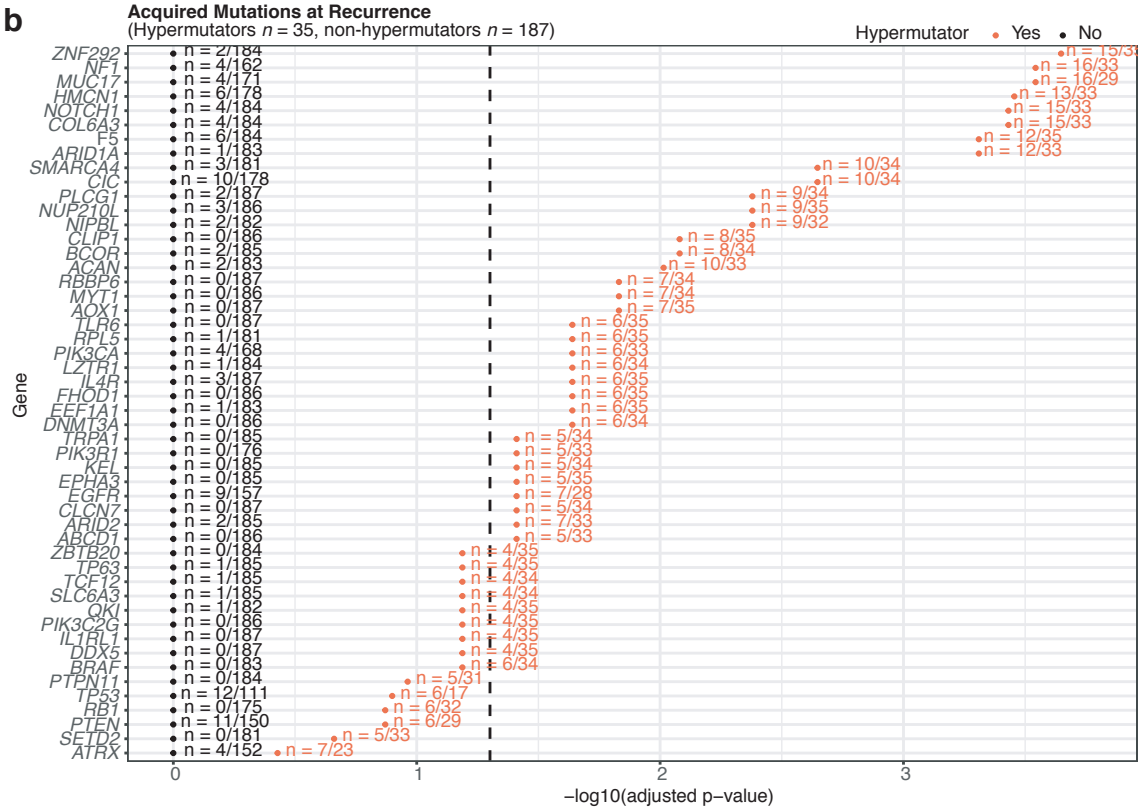

Extended Data Fig. 8 | Driver acquisition over time a. Tabulated numbers of SNV (top) and CNV (bottom) driver events that were shared, initial-only, or recurrence-only. P-values were obtained using a two-sided Fisher test comparing the initial-only fraction to the recurrence-only fraction testing for acquisition. b. One-sided Fisher test comparing the initial-only fraction to the recurrence-only fraction amongst previously implicated glioma drivers testing for driver acquisition. P-values were adjusted for multiple testing using the FDR (x-axis). Hypermutators (red) and non-hypermutators (black) were separately analyzed.

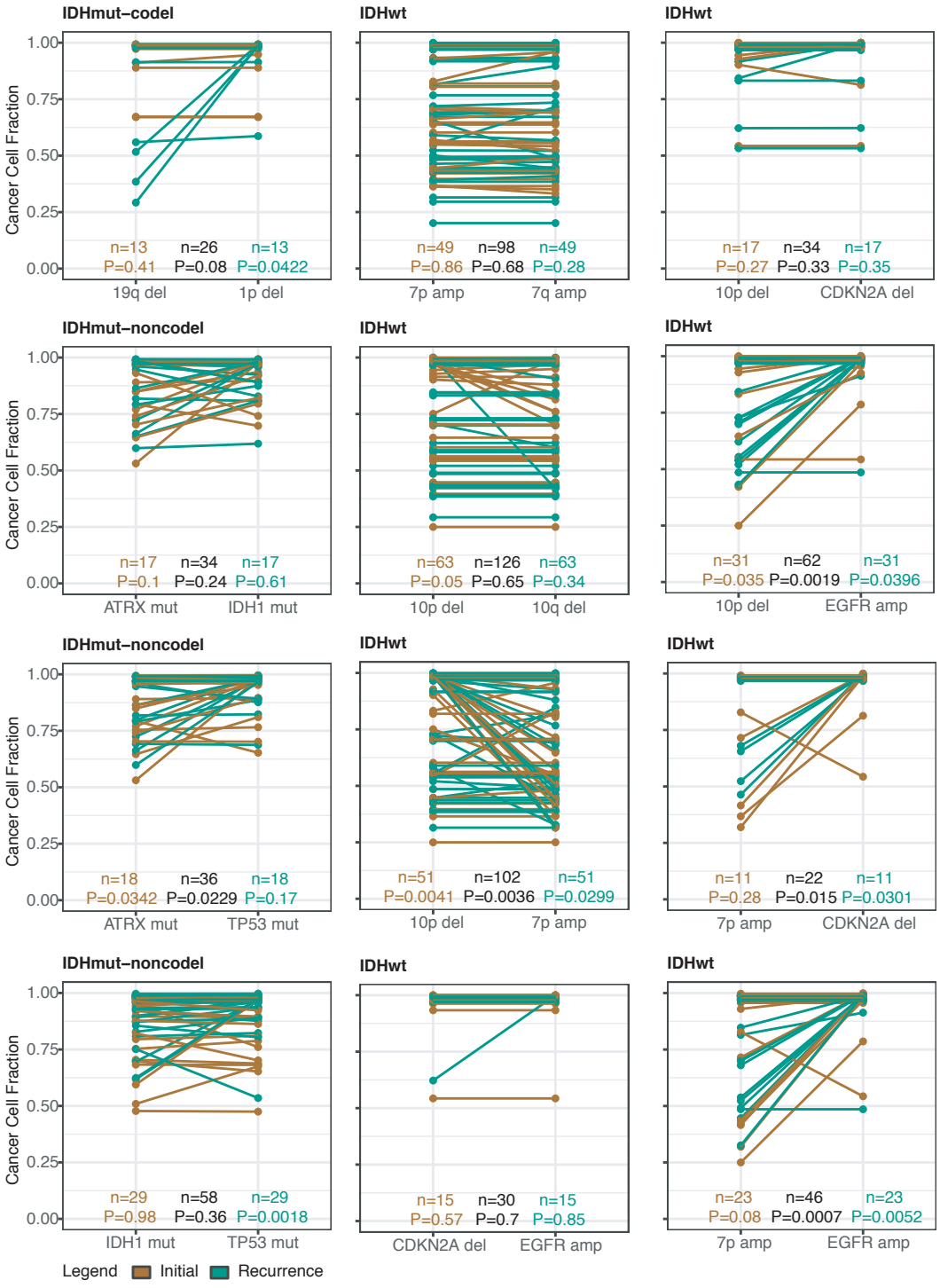

Extended Data Fig. 9 | Intra-tumor CCF comparison. Ladder plots comparing the CCF of co-occurring drivers in single tumor samples. The color of the lines and points indicates whether the sample shown is an initial (brown) or recurrent (green) tumor. Two-sided Wilcoxon rank-sum test P-values are shown for all initial samples, all recurrent samples, as well as all samples (black).

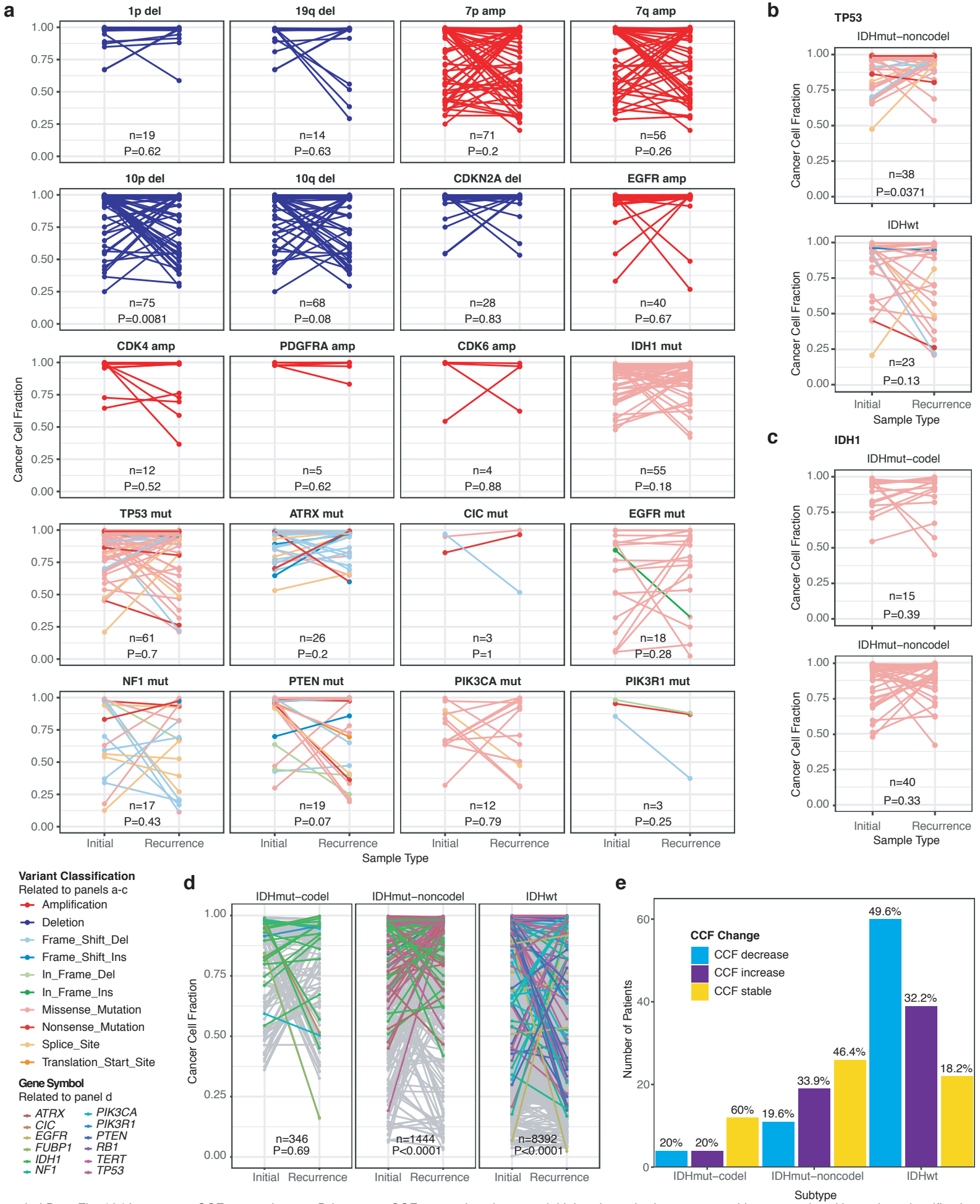

Extended Data Fig. 10 | Inter-tumor CCF comparison. a. Driver-gene CCF comparison between initial and matched recurrences. Lines are colored by variant classification. Two-sided Wilcoxon rank-sum test P-values are shown. b. TP53 CCF by subtype, otherwise as in (a). c. IDH1 CCF by subtype, otherwise as in (a). d. Ladder plot visualizing CCF change across all SNVs between initial and recurrent tumors, separated by subtype. Wilcoxon rank-sum test was used to test for differences between time points. e. Initial and recurrent mutations in each patient were compared using a Wilcoxon rank-sum test. Bar plot with counts of patients in each subtype are shown. Patients lacking significant change are shown in yellow, those with a significant increase or decrease are shown in dark and light blue, respectively.

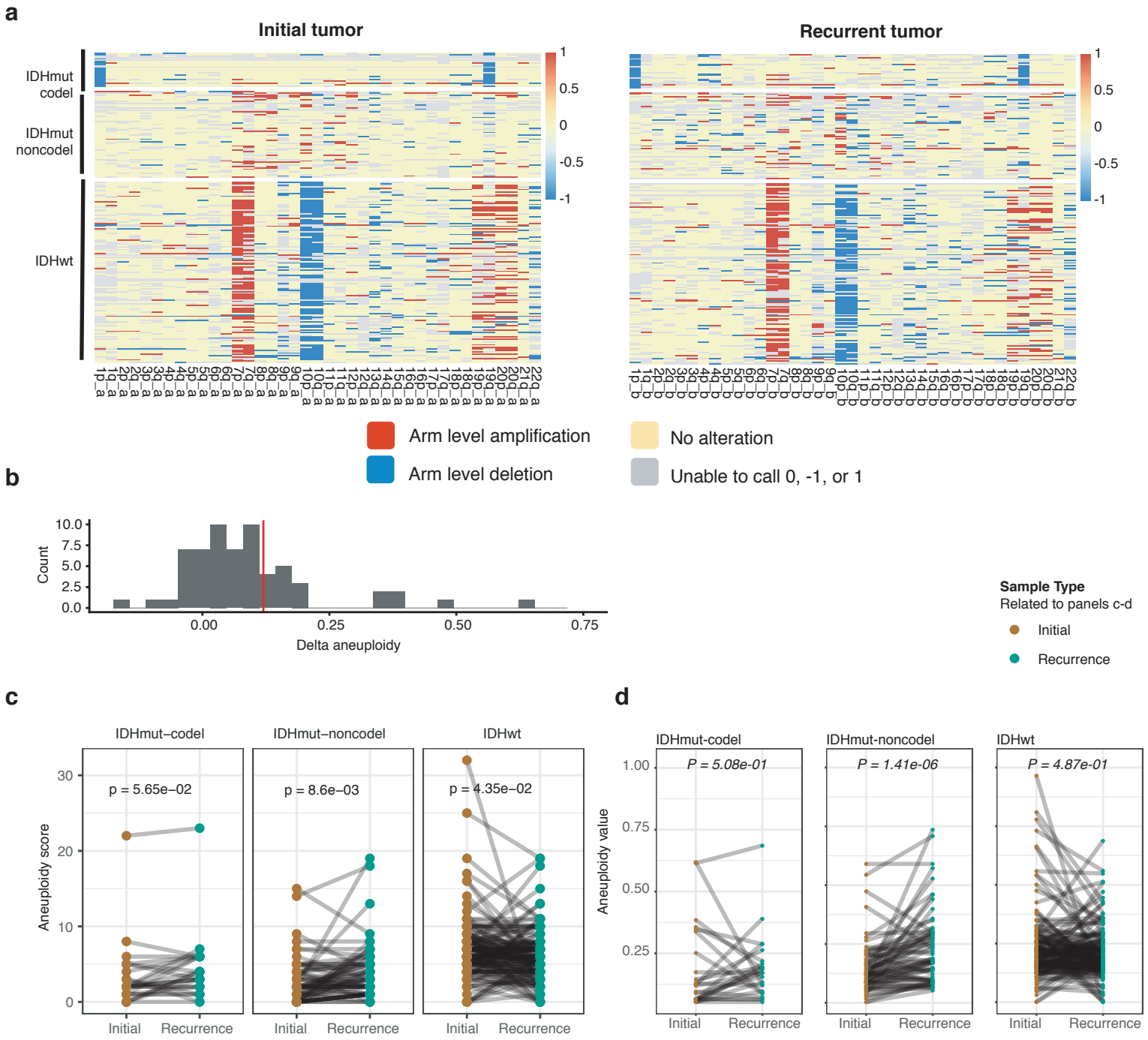

Extended Data Fig. 11 | Aneuploidy calculation a. Heatmap displaying the chromosomal arm-level events (x-axis) with patients represented in each row. Patients are placed in the same order for both the initial (left) and recurrence (right). White space was inserted as a break between the three subtypes. b. Distribution of total aneuploidy difference. Acquired aneuploidy determination (upper-quartile) indicated with a red line. c. Comparison of aneuploidy score between initial and recurrent tumors separated by subtype d. As (c), comparing aneuploidy value.

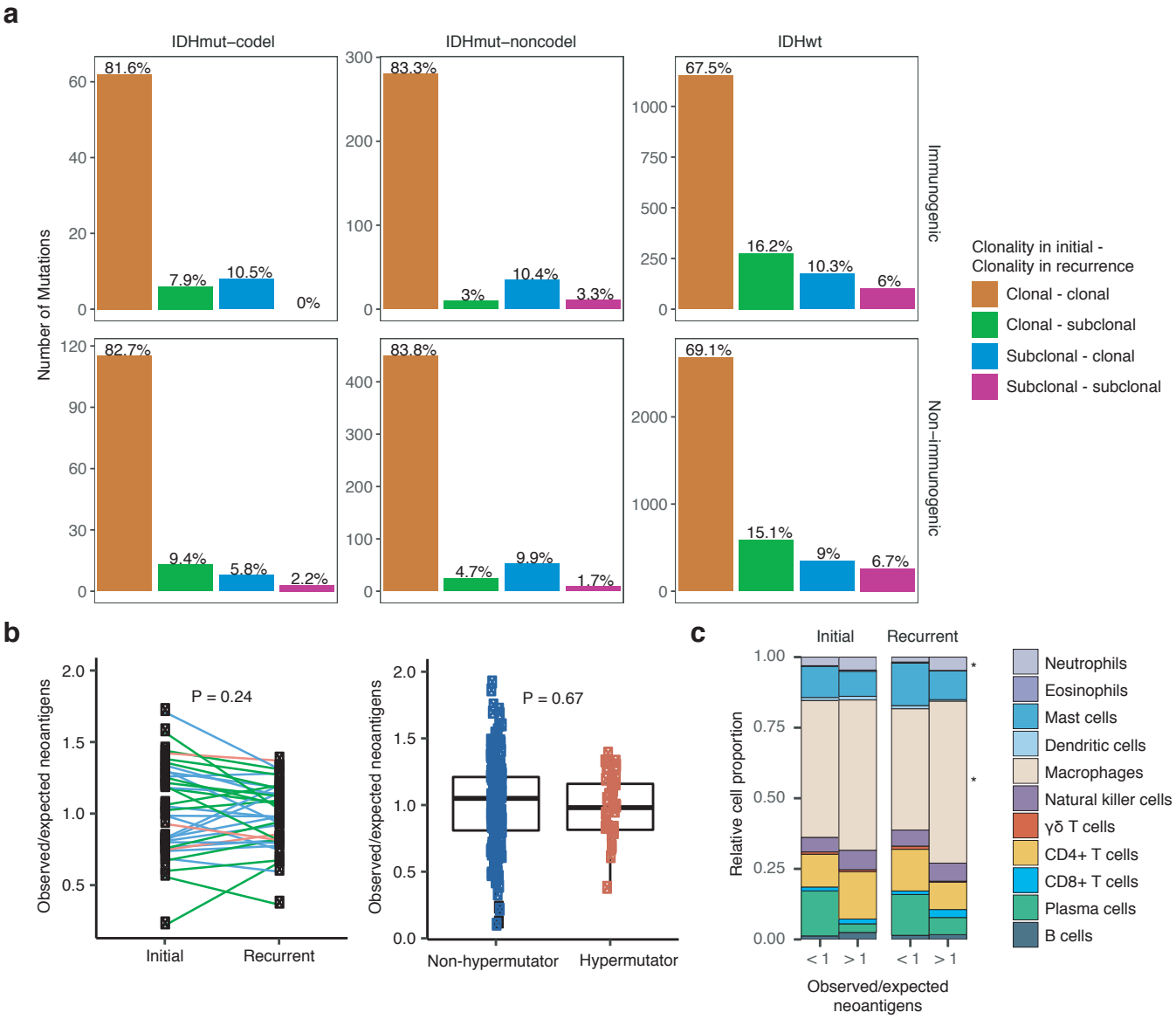

Extended Data Fig. 12 | Neoantigen evolution and cellular analysis a. Bar plots present the number of shared mutations that give rise to neoantigens (top row, “immunogenic”) and those that do not give rise to neoantigens (bottom row, “non-immunogenic”) broken down by longitudinal clonality (“(clonality in initial)-(clonality in recurrence)”) and separated by subtype. Percentage of longitudinal clonality per subtype and mutation immunogenicity are presented above the respective bars. b. Left: Ladder plot depicting the difference in observed to expected neoantigen ratio between the initial and recurrent tumors of patients with hypermutated tumors at recurrence. Each set of points connected by a line represents one tumor (n =70). Right: Boxplot depicting the distribution of observed to expected neoantigen ratios in recurrent tumors stratified by hypermutator status (n = 35 and 183 for hypermutators and non-hypermutators, respectively). Each box spans quartiles, with the lines representing the median ratio for each group. Whiskers represent absolute range, excluding outliers. P-values for panel b were calculated using the Wilcoxon rank-sum test. c. Stacked bar plots depicting the average relative fraction of 11 CIBERSORT cell types in the neoantigen depleted (< 1) and non-depleted (> 1) initial and recurrent tumor subgroups. Asterisks indicate a significant difference between the depleted and non-depleted groups for that cell type at that time.